

Review

CO₂ Electroreduction over Metallic Oxide, Carbon-Based, and Molecular Catalysts: A Mini-Review of the Current Advances

Hassan Ait Ahsaine ^{1,*} , Mohamed Zbair ^{2,3} , Amal BaQais ⁴  and Madjid Arab ^{5,*} 

¹ Laboratoire de Chimie Appliquée des Matériaux, Faculty of Sciences, Mohammed V University in Rabat, Rabat 1014, Morocco

² Mulhouse Materials Science Institute (IS2M), Université de Haute-Alsace, CNRS, UMR 7361, F-68100 Mulhouse, France; mohamed.zbair@uha.fr

³ Département de Chimie, Université de Strasbourg, F-67000 Strasbourg, France

⁴ Department of Chemistry, College of Science, Princess Nourah Bint Abdulrahman University, P.O. Box 84428, Riyadh 11671, Saudi Arabia; aabaqais@pnu.edu.sa

⁵ Aix Marseille Univ, Univ Toulon, CNRS, IM2NP, CS 60584, CEDEX 9, F-83041 Toulon, France

* Correspondence: h.aitahsaine@um5r.ac.ma (H.A.A.); madjid.arab@univ-tln.fr (M.A.)

Abstract: Electrochemical CO₂ reduction reaction (CO₂RR) is one of the most challenging targets of current energy research. Multi-electron reduction with proton-coupled reactions is more thermodynamically favorable, leading to diverse product distribution. This requires the design of stable electroactive materials having selective product generation and low overpotentials. In this review, we have explored different CO₂RR electrocatalysts in the gas phase and H-cell configurations. Five groups of electrocatalysts ranging from metals and metal oxide, single atom, carbon-based, porphyrins, covalent, metal–organic frameworks, and phthalocyanines-based electrocatalysts have been reviewed. Finally, conclusions and prospects have been elaborated.

Keywords: electrocatalysis; CO₂ reduction; molecular electrocatalysts; CO₂ conversion



Citation: Ait Ahsaine, H.; Zbair, M.; BaQais, A.; Arab, M. CO₂ Electroreduction over Metallic Oxide, Carbon-Based, and Molecular Catalysts: A Mini-Review of the Current Advances. *Catalysts* **2022**, *12*, 450. <https://doi.org/10.3390/catal12050450>

Academic Editor:
Consuelo Alvarez-Galvan

Received: 11 March 2022

Accepted: 13 April 2022

Published: 19 April 2022

Publisher's Note: MDPI stays neutral with regard to jurisdictional claims in published maps and institutional affiliations.



Copyright: © 2022 by the authors. Licensee MDPI, Basel, Switzerland. This article is an open access article distributed under the terms and conditions of the Creative Commons Attribution (CC BY) license (<https://creativecommons.org/licenses/by/4.0/>).

1. Introduction

Carbon dioxide (CO₂) is the most well-known greenhouse gas, which is produced both naturally and artificially. It is also required for the growth of all plants on the planet, as well as many industrial operations [1]. In an ideal world, CO₂ generated on Earth would be balanced by CO₂ consumed, ensuring that CO₂ levels remain constant and environmental stability is maintained. Unfortunately, as human industrial activities have become more intense, this equilibrium has been broken, resulting in increased CO₂ generation and making global warming an urgent concern. As a result, limiting CO₂ production and turning CO₂ into usable materials appears to be vital, if not critical, for environmental protection, and numerous governments throughout the world have shown their concern by boosting research funding to address the CO₂ problem. Numerous research studies have focused on the development and implementation of renewable energy sources as a way to reduce reliance on fossil fuels [2,3], as well as CO₂ capture and utilization technologies. CO₂ usage would minimize greenhouse gas emissions in the atmosphere and seas, where they might cause harm, and CO₂ could also be utilized to make valuable compounds [4–6].

As CO₂ is the most thermodynamically stable carbon molecule, it needs a lot of energy to transform into value-added compounds. Various chemical reactions have been described that can convert CO₂ into compounds such as CO, hydrocarbons, or oxygenated hydrocarbons. Gas-phase reactions, liquid-phase reactions, electrochemical reactions, and photocatalytic reactions have all been described. Gas-phase activities include dry reforming of methane (CH₄ + CO₂ → 2CO + 2H₂) and hydrogenation of CO₂ (CO₂ + H₂ → CO + H₂O, commonly known as the water-gas shift reversal reaction;

$\text{CO}_2 + 4\text{H}_2 \rightarrow \text{CH}_4 + 2\text{H}_2\text{O}$). The liquid phase technique uses CO_2 dissolved in an aqueous phase ($\text{CO}_2(\text{aq}) + \text{H}_2(\text{aq}) \rightarrow \text{COOH}$) to make formic acid. Several review studies on CO_2 hydrogenation have been published [5–8]. The hydrogenation of CO_2 or the synthesis of formic acid, on either side, necessitates H_2 , which is most typically generated from methane by steam reforming, which also generates a significant quantity of CO_2 .

Although electrochemical CO_2 reduction has garnered a lot of interest recently, the poor solubility of CO_2 in aqueous solutions has been a major impediment. The use of a gas diffusion electrode has made it possible to employ gaseous CO_2 directly for electrochemical conversion. H_2 is not required as a reactant in this electrochemical conversion process. The electrochemical reduction of CO_2 is not only a practical way to utilize CO_2 , but also a promising future alternative for storing intermittent energy from renewable sources, since it allows electrical energy to be stored in the form of chemical bonds. Carbon monoxide (CO), formic acid (HCOOH), formaldehyde (CH_2O), methanol (CH_3OH), methane (CH_4), ethanol ($\text{C}_2\text{H}_6\text{O}$), ethylene (C_2H_4), or n-propanol ($\text{C}_3\text{H}_8\text{O}$) are some of the important byproducts of CO_2 electroreduction [1,8]. The hurdles of converting CO_2 to CH_3OH are particularly daunting, but the potential benefits are huge, as CH_3OH has a very high energy density and is a crucial intermediary for various bulk chemicals used in everyday items such as silicone, paints, and plastics [9,10].

In addition, the majority of electrodes used in CO_2 electroreduction are metal plates, metal granules, or electrodeposited metals on a substrate [1]. The mass transfer of CO_2 from the bulk to the solid electrode surface, however, is limited by the comparatively low solubility of CO_2 in water under ambient circumstances, thus limiting the reaction rates and current densities of CO_2 electroreduction [11,12].

This review highlights the recent progress in the field CO_2 electroreduction including the use of gas diffusion electrode configuration (GDE). We have reviewed the different electrode materials ranging from oxides, metallic and bimetallic, carbon-based materials, single-atom catalysts, and molecular catalysts (porphyrins, metal–organic frameworks, covalent organic frameworks, and phthalocyanines) for the CO_2 reduction to C_1 and C_2 chemicals. The effect of several parameters was discussed.

2. Electrocatalytic CO_2 Reduction

2.1. Oxide, Metallic, and Bimetallic Catalysts

The use of gas-diffusion electrodes (GDEs) reduces CO_2 by pouring pure CO_2 gas onto the catalytic layer of the GDE, delivering it onto the cathode without being dissolved in catholyte in gas-phase electrolysis of CO_2 . A porous composite electrode, or GDE, is typically made up of polymer-bonded catalyst particles and carbon support. Higher current densities (200–600 mA cm^{-2}) may be achieved using GDEs. Furthermore, due to their high porosity and partial hydrophobicity, GDEs create a unique gas–solid–liquid three-phase interface, allowing for a uniform dispersion across the catalytic surface. Because of these characteristics, GDEs are particularly well suited to CO_2 electroreduction in the gas phase [13–16]. Janaky's group has reported an important study on the comparison of the operation of electrolyzer cells using different anode materials. The authors showed that while Ir is stable under process conditions, the degradation of Ni leads to a rapid cell failure [17]. The same group has also shed light on other anodic oxygen evolution catalysts that are also detrimental to good GDEs stability during a CO_2RR reaction [18]. Electrocatalytic reduction is frequently plagued by high overpotential, poor kinetics, limited product selectivity, and catalyst stability [19–21]. Noble metal electrodes provide great selectivity and stability for CO_2 reduction at low over-potential [22–25]. Furthermore, catalysts based on low-cost materials, such as Sn [26–28], Cu [29,30], Co [31–33], and carbon compounds [34–36], are being investigated. CO is the most common result of carbon dioxide reduction reactions (CO_2RR), and it is produced by Au, Ag, Zn, and Pd [37]. CO is a significant chemical feedstock for a variety of chemical reactions [16]. The binding energy of $^*\text{COOH}$ is a critical characteristic for CO generation. The metals bind to $^*\text{COOH}$ in a sequential manner, generating $^*\text{CO}$ following dehydration [38–40]. The CO reaction

pathway consumes two electrons and is quite simple [38]. When CO is the major product, there is no need to separate the gaseous CO from the liquid electrolyte because it will spontaneously separate. To this date, we can rank three distinct groups of monometallic catalysts: (1) CO selective metals such as (Au, Ag, Pd, Ga, and Zn) [41,42]; (2) metals that mainly produce HCOOH (e.g., Pb, Cd, Sn, In, and Ti) [43–46]; (3) metals that form hydrocarbons such as CH₄ and C₂H₄ (e.g., Cu) [47].

Numerous investigations attempting to control the nanostructures of these metals have been known to have high CO production from CO₂RR, such as concave rhombic dodecahedral Au nanoparticles with high-index facets [48], TiC-supported Au nanoparticles [49], hexagonal Zn particles [50], electrodeposited Zn dendrites [51], Au electrode with adsorbed CN[−] or Cl[−] ions [52], Ag nanoparticles with surface-bonded oxygen [53], monodispersed Au or Ag nanoparticles [54,55], ligand-free Au nanoparticles with < 2 nm [56], and inverse opal Au or Ag thin films [57,58]. Although it is difficult to evaluate their performance due to the differences in reaction circumstances, CO₂ to CO conversion typically achieves 90 to 100 percent Faradaic efficiency at a modest overpotential of 0.4 to 0.7 V. Kanan's group [59] has reported remarkable locally enhanced CO₂ reduction on gold electrode by studying the influence of bulk defects. These latter appeared to affect the faradaic efficiency and selectivity during CO₂ reduction. The same group has also reported the production of formate on SnO_x with a Faradaic efficiency of 58% compared to tin foil only ~19%. The recorded current density of 1.8 mA cm^{−2} was achieved at −0.7 V vs. RHE [26].

Vasileff et al. [37] discussed and reviewed the surface and interface of copper-based-bimetallic toward CO₂ electroreduction. Au has been the most typical group 1 metal alloyed with Cu for the CO₂RR because it is a d-block metal with poor hydrogen and oxygen adsorption. Increased Au concentration encouraged CO generation, and the route to CH₄ was restricted, according to the Christophe study [60]. CO desorption on Cu sites was aided by the decreased activation energy for CO desorption generated by Au alloying on a mechanistic level. In another study, it was discovered that the composition and nanostructure of Cu–Au nanoparticles influenced catalytic performance, resulting in the selective production of CH₃OH and C₂H₅OH [61].

The Faradaic efficiency (FE) for alcohols in the ideal Cu_{63.9}Au_{36.1} mixture was 28% (including 15.9% for CH₃OH), which is 19 times greater than that of pure Cu. This study stated that *CO is a key intermediary in the conversion of CO₂ to hydrocarbons and alcohols and that the binding of *CO in this Cu–Au system was likely optimized [62]. Electrochemical results from a comprehensive examination into the effect of the Cu–Au stoichiometric ratio in bimetallic catalysts revealed that alloys with higher Cu content obtained various reduction products, whereas alloys with higher Au content improved CO formation while suppressing other pathways. Cu–Au alloys were shown to enhance CO generation due to their synergistic electrical and geometric effects. The d-band center drops downwards from pure Cu to pure Au, according to density functional theory (DFT) calculations (Figure 1a). As a result, as the Au content increases, the binding strength for *COOH and *CO should decrease, and the generation of CO in Cu–Au systems should follow a monotonic pattern (Figure 1b); however, because of a geometric effect that stabilized *COOH intermediates, *COOH binding was shown to be substantially unaffected. This justifies their experimental outcomes, which show that the Au₃Cu alloy has the highest FE toward CO (Figure 1c), and it gives them a better understanding of the implications of electronic structure and geometric change in bimetallic materials. Furthermore, raising the degree of atomic ordering in Cu–Au alloys was discovered to control the selectivity of CO₂ reduction toward CO with a high FE of 80%, which is attributed to the stability *COOH intermediates on compressively strained Au sites [63].

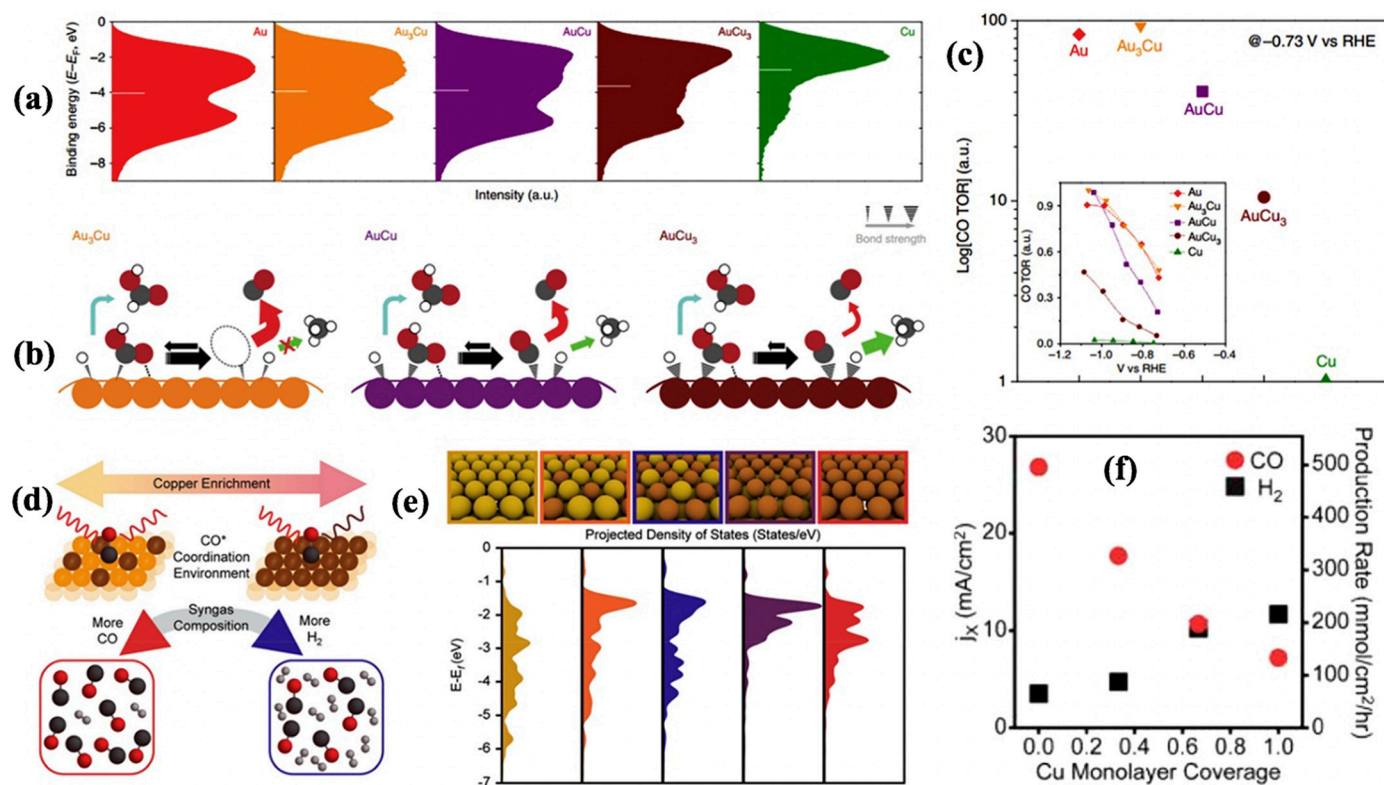


Figure 1. Characterization and performance of Cu–Au catalysts for the CO₂RR. (a–c) Surface valence-band photoemission spectra of Au–Cu bimetallic nanoparticles (the white bars indicate the d-band centers) (a); proposed mechanism for the CO₂RR on the surface of Au–Cu bimetallic nanoparticles (gray, red, and white atoms represent C, O, and H, respectively) (b); CO generation rate on various alloy electrocatalysts at a certain overpotential (inset shows relative CO generation rate as a function of the applied potential) (c). (Reprinted with permission from Ref. [51]. Copyright 2015 American Chemical Society). (d–f) Scheme depicting the relationship between the Cu-enriched Au surface, in situ characterization of CO* coordination, and syngas composition (d); calculated d-band electronic states for increasingly Cu-enriched Au surfaces (e); partial current densities (left axis) and production rates (right axis) for CO and H₂ as a function of Cu monolayer deposition on Au (f). (Reprinted with permission from Ref. [64]. Copyright 2017 American Chemical Society).

By depositing a single layer of Cu with varying coverages, Ross et al. created another form of Cu–Au alloy [64]. They discovered that lower Cu coverage enhanced CO generation, whereas higher Cu coverage promoted H₂ evolution. They studied the impact of the Cu/Au ratio on the *CO adsorption strength using in situ Raman microscopy and the vibration of the C–O bond in *CO species as a descriptor. The red shift in vibration of C–O was shown to be linked with bond lengthening due to increased metal contact (Figure 1d). Figure 1e shows that on more Au-dominant surfaces, the projected density of states (DOS) went farther away from the Fermi level, favoring CO generation (DFT calculations). Cu enrichment, on the other hand, improved the adsorption of *H more than it did for *CO. As a result, the degree of Cu enrichment can modify the HER's relative activity to the CO₂RR, allowing for the generation of tunable syngas (Figure 1f). Experiments in a Au–Cu core-shell (Au@Cu) system revealed that seven to eight layers of Cu resulted in greater selectivity for C₂H₄, but CH₄ generation rose somewhat for 14 or more Cu layers [65]. The computed DFT findings revealed that on terraces, *COH intermediates were preferred over *CHO; but, as *CO coverage rose, *CHO was somewhat favored [66]. As a result, structural and electrical factors that modify the binding of *CO on Au@Cu catalysts have a considerable impact on selectivity and product distribution. In another work, Cu–Au

core-shell nanostructures (Cu@Au) had a higher FE toward CO and had a higher current density than polycrystalline Cu [67].

Contemporary research has found that oxide-derived metal electrodes outperform virgin metal electrodes in terms of catalytic performance [68]. The most typical method for making oxide-derived electrocatalysts is to oxidize the metal before reducing it to its original metallic form. At the same overpotential, oxide-derived Cu generated more C₂ products of C₂H₄, C₂H₆, and ethanol than electropolished Cu [68–70]. Cl ion-adsorbed oxide-derived Cu [71] yielded C₃ and C₄ products of C₃H₇OH, C₃H₆, C₃H₈, and C₄H₁₀. For the synthesis of formic acid, oxide-derived Sn had a substantially greater current density and Faraday efficiency than a pure Sn electrode [72]. As shown in Figure 2a, oxygen-derived Au [73] or Ag [74] had a higher FE for CO generation, ranging from 90 to 100 percent at only 0.3 V overpotential.

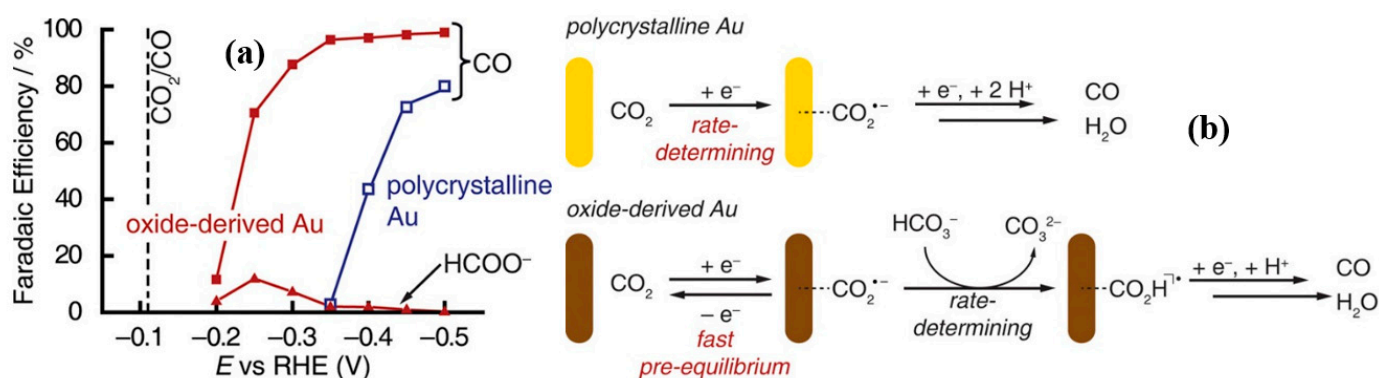


Figure 2. (a): FEs for CO and HCO₂⁻ production on oxide-derived Au and polycrystalline Au electrodes at various potentials between −0.2 and −0.5 V in 0.5 M NaHCO₃, pH 7.2. Dashed line indicates the CO equilibrium potential. (b): suggested mechanisms for CO₂ reduction to CO on polycrystalline Au and oxide-derived Au (Reprinted with permission from Ref. [74]. Copyright 2016 Wiley-VCH).

The origin of the increase in oxide-derived metals for CO₂RR has been a point of conflict. The source of the strengthening has been proposed to be nanostructures produced in the catalysts or residual subsurface oxygen. After oxidation-reduction cycling, nanostructured surfaces with rich grain boundaries were formed [75,76]. More defect sites with greater binding energy to *CO and higher local pH were found on the induced surface, which improved selectivity toward CO₂RR while reducing HER [76–78]. Despite the CO₂RR's extremely decreased circumstances, it was also hypothesized that some oxygen persisted in the subsurface. As demonstrated in Figure 2b [79,80], ambient pressure XPS, in situ electron energy loss spectroscopy examinations, and DFT simulations revealed that oxygen assisted in the early activation of CO₂ on the surface; however, a conflicting conclusion was also published, claiming that under the CO₂RR situation, the remaining oxide was highly unstable and the amount of oxygen was insignificant [81].

Commercial Cu₂O and Cu₂O–ZnO mixes coated on carbon sheets have been used by Albo et al. [82] to make gas-diffusion electrodes, which are tested in a filter-press electrochemical cell for continuous CO₂ gas-phase electroreduction (Figure 3). The operation mostly yielded methanol, with minor amounts of ethanol and n-propanol. The investigation uses a 0.5 M KHCO₃ aqueous solution to measure critical variables affecting the electroreduction process: current density ($j = 10\text{--}40 \text{ mA cm}^{-2}$), electrolyte flow/area ratio ($Q_e/A = 1\text{--}3 \text{ mL min}^{-1} \text{ cm}^{-2}$), and CO₂ gas flow/area ratio ($Q_g/A = 10\text{--}40 \text{ mL min}^{-1} \text{ cm}^{-2}$). At an applied potential of 1.39 and 1.16 V vs. Ag/AgCl, respectively, the greatest CO₂ conversion efficiency to liquid-phase products was 54.8 percent and 31.4 percent for Cu₂O and Cu₂O/ZnO-based electrodes.

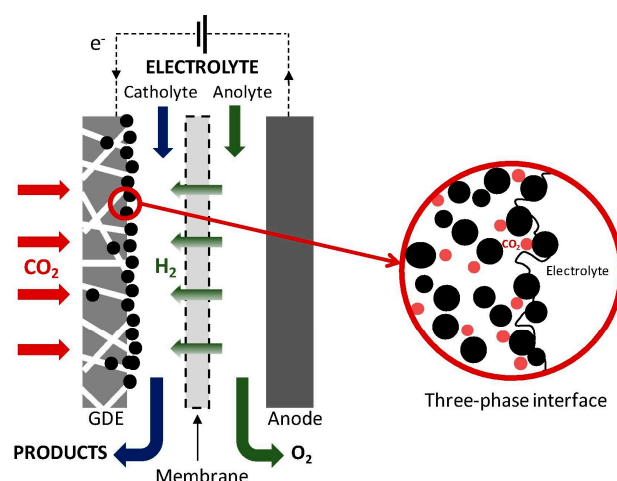


Figure 3. Representation diagram of the electrolytic cell configuration for the electroreduction of CO₂ supplied directly from the gas phase. In this study, the filter-press electrochemical system possesses three inputs (catholyte, anolyte, and CO₂ separately) and two outputs (catholyte–CO₂ and anolyte) for the electroreduction of CO₂ in gas phase. (Reprinted with permission from Ref. [82]. Copyright 2016 Elsevier).

2.2. Single-Atom Catalysts

Single-atom catalysts (SAC) are metal catalysts that are atomically scattered on the surface of a support. They have unusual selectivity and have extremely different electronic structures and adsorption patterns of reactants and intermediates [83]. Electrochemical CO₂RR [84] has been studied using SACs. As shown in Figure 4 [84], Ni single atoms on N-doped graphene can selectively catalyze CO₂RR and produce CO. Various metal atoms with quite different d-band structures, such as Fe, Co, Mn, and Cu, have demonstrated varying selectivity. The electronic structure and binding energy of important carbon intermediates have been found to be affected by the coordination environment around the Ni single atom [85,86]. Cu Ion-O vacancy pairs formed when Cu was atomically doped into CeO₂, and the oxygen defect sites of CeO₂ governed copper's oxidation state. CO₂RR was catalyzed by a single atomic Cu, which produced CH₄ with a 58 percent Faraday efficiency [87]. With the right metal atoms and supports, DFT calculations predict that the SAC structure can suppress HER while promoting CO₂RR [88,89]. Computational methods have also suggested single-atom alloys, in which a single-atomic metal is located on another metal surface, as effective CO₂RR catalysts [90].

Pan and coworkers have developed a Co-N₅ single atom through pyrolysis and wt impregnation method for the electrocatalytic reduction of CO₂ to Co, reaching a Faradaic efficiency of 99% at -0.73 V vs. RHE at a current density of 6.2 mA cm^{-2} . The Co SAC was stable for 10 h of electrolysis [33]. Another Co single atom (Co-N₂) has been reported by [91] from the pyrolysis of Co/Zn MOF; this electrocatalyst achieved a Faradaic efficiency for CO₂ reduction of 94% at -0.63 V vs. RHE and a current density of 18.12 mA cm^{-2} . This catalyst had a steady-state stability of 60 h. Iron single atoms have also been reported for CO₂ electroreduction; for instance, Pan and coworkers [92] have recently reported Fe-N-C prepared from Fe salt, Zn salt, and 2-methylimidazole. The prepared material was evaluated for CO₂-to-CO with a selectivity of 93% at -0.7 V vs. RHE and a current density of 2.8 mA cm^{-2} . This Fe SAC showed a steady-state CO evolution for 20 h. Zhang et al. [93] have synthesized an Fe/NG SAC electrocatalyst using Lyophilization and reduction of the precursors (Graphene oxide and Iron salt). The Fe/NG SAC yielded 80% Faradaic efficiency for CO and stability of 10 h.

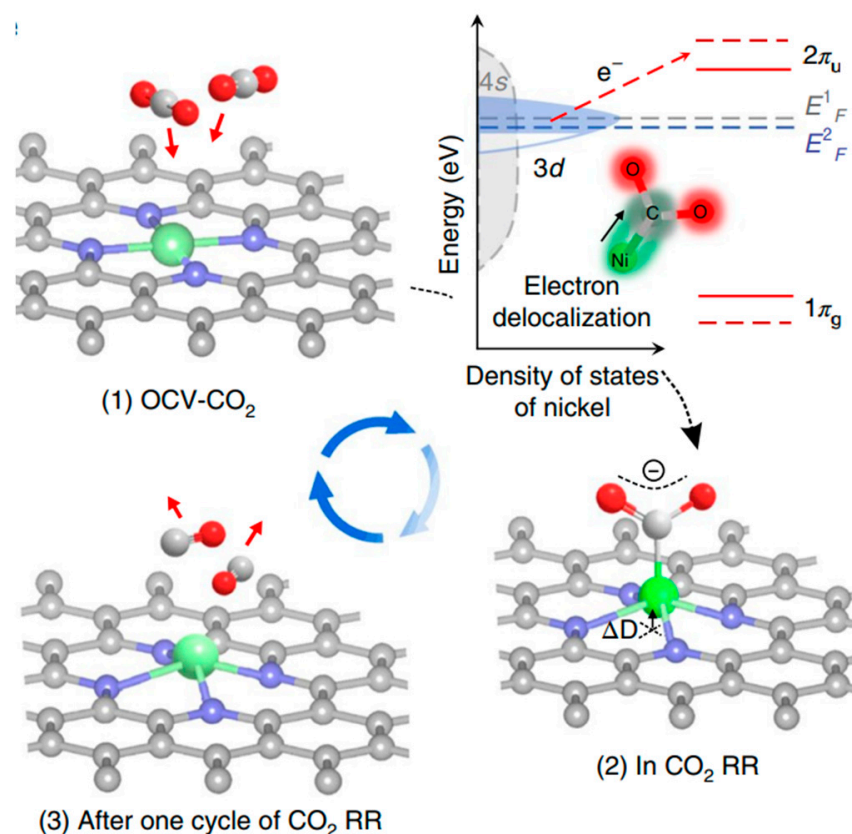


Figure 4. Structural evolution of Ni single-atom sites on graphene during CO₂RR. ΔD in shows the displacement of Ni atom out of plane resulting from electron transfer from Ni atom to CO₂. The upper-right schematic shows the activation processes for CO₂ molecules on the Ni(i) site. A valence band structure, similar to metallic nickel, was used to simplify the schematic illustration. The red arrow represents the electron transfer from the Ni(i) to adsorbed CO₂. E_F^1 and E_F^2 are Fermi levels of A-Ni-NG before and after formation of Ni-CO₂, respectively. $1\pi_g$ and $2\pi_u$ are CO₂ molecular orbitals. (Reprinted with permission from Ref. [84]. Copyright 2018 SpringerNature).

In a CO₂-saturated 0.1 M KHCO₃ solution, the electrocatalytic performance of Cu-CeO₂ nanorod samples was evaluated [87]. CV curves of Cu-CeO₂-4% nanorods, undoped CeO₂ nanorods, and Cu nanoparticles vs. a reversible hydrogen electrode (RHE, Figure 5a) were measured in a potential window between -0.2 and -1.8 V. Because CeO₂ has a lower electrical conductivity than Cu, the Cu-CeO₂-4% nanorods (red curve) have a lower total current density (j_{tot}) than pure Cu (blue curve), although they are still much greater than CeO₂ (black curve). Figure 5b–d show the electrocatalytic reduction products of these three catalysts as determined by in-line gas chromatography (GC) and ¹H nuclear magnetic resonance (NMR). Cu-CeO₂ nanorods had a much smaller quantity of H₂ side products from water reduction (gray columns in Figure 5b–d) and a significantly higher number of electrocatalytic CO₂ reduction products than Cu nanoparticles and undoped CeO₂ nanorods, showing strong CO₂ reduction activity on the Cu-doped CeO₂ electrocatalysts. The current densities for all deep reduction products (j_{drp}) were computed and plotted by multiplying j_{total} and the corresponding FEs for all deep reduction products (i.e., CO₂ reduction products excluding CO and HCOO⁻) (Figure 5b–d, red y -axis on the right). At -1.6 , -1.8 , and -2.0 V versus RHE, the j_{drp} of the Cu-CeO₂-4% nanorods reaches 40, 70, and 90 mA cm⁻² (based on geometric surface area), which was many times greater than the pure Cu and undoped CeO₂ samples.

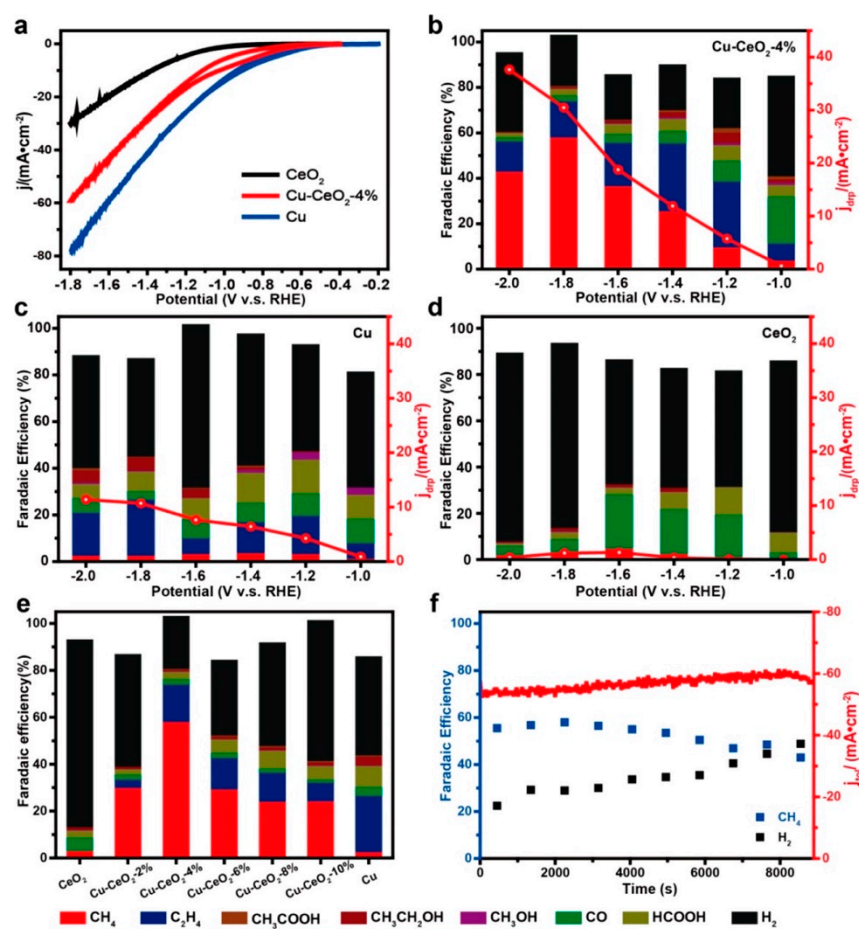


Figure 5. Electrochemical CO₂ reduction performance. (a) Cyclic voltammograms for Cu-CeO₂, CeO₂, and Cu. (b–d) Faradaic efficiencies (bars on the left y -axis) and deep reduction product current density (j_{drp} , red curves on the right y -axis) of (b) Cu-CeO₂-4%, (c) pure Cu, and (d) undoped CeO₂ at various overpotentials. The deep reduction products were the first five products in the legends at the bottom, marked with a red line. (e) A comparison of the Faradaic efficiency of samples with varying levels of Cu doping. (f) Stability of FE_{CH₄} (blue squares) and FE_{H₂} (black squares) on the left y -axis. Right y -axis: total current density (j_{total}) of Cu-CeO₂-4% at -1.8 V (red curves, right y -axis). (Reprinted with permission from Ref. [87]. Copyright 2018 American Chemical Society).

2.3. Carbon-Based Catalysts

Carbon-based materials are being investigated as potential electrocatalysts for electrochemical processes such as the oxygen reduction reaction (ORR), the oxygen evolution reaction (OER), and the hydrogen evolution reaction (HER) [94,95]. Carbon materials provide a number of benefits for electrochemical applications, including the capacity to be easily transformed into different sizes and forms [96]. Well-developed material science techniques may be used to create zero-dimensional carbon dots, graphene quantum dots, one-dimensional carbon nanotubes, two-dimensional graphene, and three-dimensional graphene aerogel [21]. Carbon materials have strong chemical and mechanical stability, as well as high conductivity and surface area.

CO₂RR is essentially inert to pure carbon compounds. Electrocatalytic activity is considerably improved when heteroatoms such as N are doped in the carbon matrix. CO₂RR considers negatively charged N sites to be active sites [97,98]. N-doping the catalyst creates a Lewis base site, which helps to stabilize CO₂ [98]. N-doped carbon nanotubes [99,100], N-doped graphene [101], and N-doped graphene quantum dots [35] are among the carbon materials that have been reported for CO₂RR through the two-

electron route. Acetate and formate with N-sp³C active sites were synthesized by N-doped diamonds [102]. CO₂RR has also been performed with other dopants, such as S or B [103,104].

Pan et al. [33] used an N-coordination technique to build a stable CO₂ reduction reaction electrocatalyst with an atomically distributed Co–N₅ site anchored to hollow N-doped porous carbon spheres made from polymers. The synthesis steps are depicted in Figure 6. The authors use a modified Stöber technique [105] to make core@shell SiO₂@melamine-resorcinol-formaldehyde polymer spheres (MRFPs). Then, by pyrolyzing SiO₂@MRFPs at 700 °C under Ar, SiO₂@N-doped porous carbon spheres were produced. The HNPCs were created after etching the silica core with HF. Finally, the CoN₅/HNPCs catalyst was developed by establishing a coordination connection between Co and N. The catalyst has a strong selectivity for CO₂ reduction, with a CO Faradaic efficiency (FE_{CO}) of more than 90% throughout a wide potential range of –0.57 to –0.88 V (the FE_{CO} approached 99 percent at –0.73 and –0.79 V). After electrolyzing for 10 h, the CO current density and FE_{CO} remained practically constant, demonstrating excellent stability. Experiments and density functional theory simulations demonstrate that the single-atom Co–N₅ site is the primary active center for simultaneous CO₂ activation, fast production of the critical intermediate COOH*, and CO desorption.

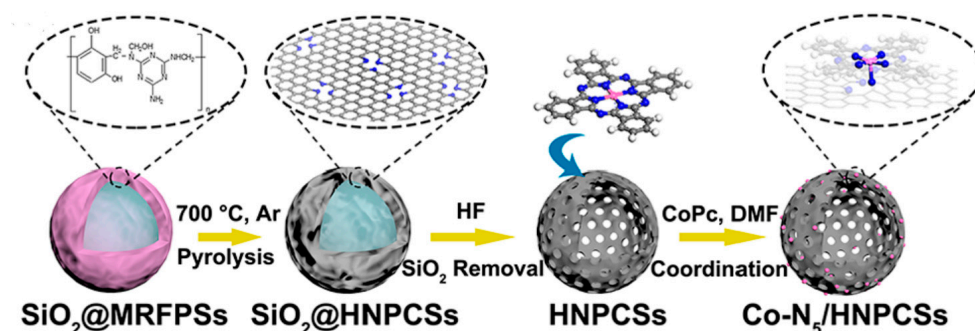


Figure 6. Schematic illustration of catalyst preparation. The core@shell SiO₂@melamine-resorcinol-formaldehyde polymer spheres (MRFPs) were first synthesized. Then, SiO₂@N-doped porous carbon spheres were obtained by pyrolysis of SiO₂@MRFPs at 700 °C under Ar. After etching the silica core with HF, the HNPCs were obtained. Finally, the Co–N₅/HNPCs catalyst was prepared through constructing coordination interaction between Co and N. (Reprinted with permission from Ref. [33]. Copyright 2018 American Chemical Society).

Carbon compounds doped with nitrogen are effective CO₂ electroreduction catalysts [21,106]. In ionic liquids, nitrogen-doped carbon nanofibers showed a modest overpotential for CO₂ reduction [36]. Although the product selectivity of each was very poor, the N-doped graphene quantum dot generated multi-carbon compounds such as ethanol, acetate, and n-propanol [35]. In aqueous conditions, nitrogen-doped mesoporous carbon was recently employed to convert CO₂ to ethanol with great efficiency and selectivity (77%) [34]. Other N-doped materials for CO₂ reduction reactions have been reported, including N-doped graphene [107,108], and carbon [109,110].

Because of their unique electrical and geometric properties [111], N-doped carbon nanotubes have attracted a lot of interest in CO₂ reduction and other electrocatalysis [112]. NCNTs modified with polyethylenimine may convert CO₂ to formate in aqueous environments with good selectivity (87%) and current density [113]. NCNT arrays produced by chemical vapor deposition (CVD) demonstrated good selectivity for CO of 80% at –0.26 V overpotential [99]. The high density of pyridinic N sites (27 percent of all Ns) in this NCNT array [100] was attributable to its superior activity. When compared to a reversible hydrogen electrode (RHE) with a pyridinic N concentration of 32%, NCNTs catalysts produced by calcination of polymers may obtain a maximum current efficiency of 90% for CO production at a potential of 0.9 V [98]. In comparison to noble-metal catalysts,

however, such NCNT catalysts have a low CO current density. For more effective catalysts, increasing the N concentration is crucial.

Pyridinic N is the most significant catalytic site for carbon dioxide reduction reactions (CO₂RR) among nitrogen-doped carbon materials. Graphitic N defects have a lower ability to bind CO₂, while pyrrolic N defects have little to no effect on CO₂RR activity; however, the atomic abundance of pyridinic N in most catalysts was low, accounting for just around 30% of all N atoms, and only a few materials could achieve a pyridinic N content of over 60%. Increasing the number of pyridinic N defects is therefore crucial. Pyrolysis is an effective method for producing high-N-content NCNTs [101,108,109].

Pyrolysis of electrospun nanofiber mats of heteroatomic polyacrylonitrile (PAN) polymer yielded a low-cost, metal-free carbon nanofiber (CNF) catalyst for CO₂ reduction [36]. This catalyst's heteroatomic structure was intended to make use of nitrogen atoms already present in the precursor's backbone (PAN). CNF catalysts include two electrochemically active species: pyridinic nitrogen and positively charged carbon atoms. To balance out the pyridinic N's high negative charge density, the adjacent carbon atom has a higher positive charge density and is an oxidized carbon. If the fascinating CO₂ conversion seen for CNFs is linked to nitrogen functional groups, the composition of nitrogen atoms should alter dramatically following the experiment. The authors [36] evaluated the change in the N atom configuration of the CNFs catalyst by recording high-resolution N1s spectra before and after the 9 h electrochemical reaction (Figure 7). In CNFs, Figure 7a shows the presence of three primary nitrogen species: pyridinic (B.E. ~398.5 eV), quaternary (B.E. ~401.1 eV), and nitrogen oxides (B.E. ~402.2 eV). The quantitative studies show that pyridinic nitrogen makes up 25.8%, quaternary nitrogen makes up 36.7 percent, and N-oxide makes up 37.5 percent of the total nitrogen. An extra prominent N peak (pyridonic nitrogen) was identified at B.E. (400.1 eV) in the N1s spectra (Figure 7b) collected for CNFs following the 9 h reaction. According to the authors, the size of the N-oxide peak reduces dramatically (37.5–10%), showing that N-oxides are transformed into pyridonic nitrogen (peak area varies from 0 to 37%). Though, the CNF catalysts' electrochemical activity stays unaltered, indicating that N-oxides were not involved in the CO₂ conversion process. Surprisingly, following the 9-h trials, the strength of the pyridinic (very active) and quaternary nitrogen (less active) peaks stays practically unchanged. Furthermore, the authors speculated that there might be two alternative processes if pyridinic nitrogen was directly involved in the reaction. First, pyridinic nitrogen may be permanently protonated, resulting in quaternary nitrogen [114], which would increase the peak area of quaternary nitrogen since the B.E. for protonated nitrogen is comparable to that of quaternary (401.3 eV) [115]. Instead of getting irreversibly protonated, pyridinic nitrogen might weakly attach to CO₂ species in a way similar to pyridine reduction, resulting in pyridinic nitrogen conversion to pyridinic species [114]. In both situations, the peak area of the pyridinic nitrogen peak would have been reduced (after tests), but it remains the same (25.8%), demonstrating that such reactions do not occur in the system. As a result, N1s spectra studies force authors to consider that positively charged carbon atoms lead to the electrochemical reduction of CO₂. This is further supported by the fact that nitrogen-free carbon atom catalysts (such as graphite) have a very low CO₂ reduction current density.

Based on theoretical [116,117] and experimental [118–120] investigations, the oxidized carbon atoms can function as excellent catalysts for reduction reactions due to their high atomic charge and spin density. The naturally oxidized carbon atoms can be decreased at first by the redox cycling mechanism. The intermediate complex [EMIM–CO₂] adsorbs on reduced carbon atoms and reoxidizes them to their original form, yielding CO as a product in the second step (Figure 7e).

Wu and coworkers [101] employed a CVD method to create microporous graphene foams, which were subsequently doped with nitrogen (N) using graphitic carbon nitride (g-C₃N₄). In terms of CO generation, the resulting N-graphene was both active and selective, with a nitrogen content of 6.5 percent. At –0.58 V vs. the reversible hydrogen electrode (RHE), which is an overpotential of –0.47 V. Formate production was also re-

ported, although at a low FE of 3% (at -0.58 V), implying that the CO_2RR on this catalyst material follows a $2e^-$ route.

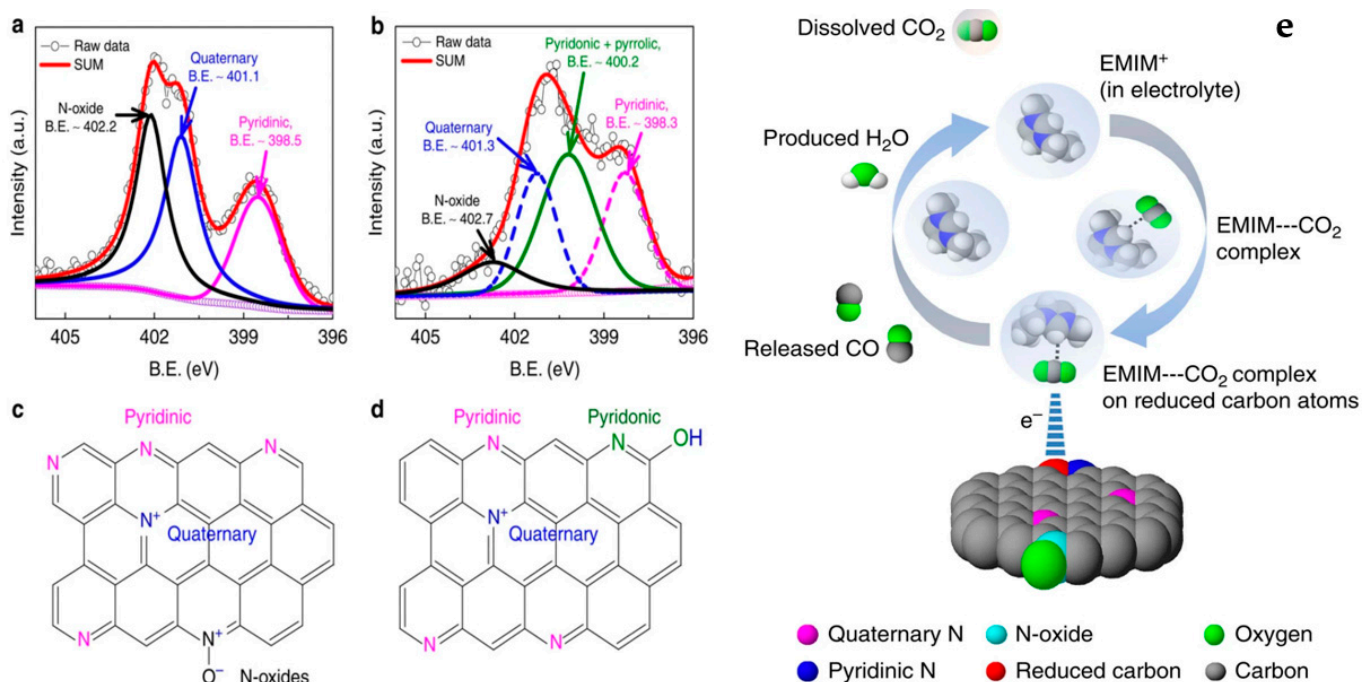


Figure 7. (a–d) Evolution of nitrogen atomic nature in CNFs by XPS. (a) Deconvoluted N1s spectra for CNFs before and (b) after electrochemical experiments. In used catalysts, CNFs N1s spectra, N-oxide type of nitrogen content reduced radically and new peak (green solid line) at 400.2 eV (pyridonic N) appears. (c,d) The corresponding atomic structure on the basis of XPS analysis. (e): CO_2 reduction mechanism schematic diagram. The CO_2 reduction reaction takes place in three steps: (1) an intermediate (EMIM– CO_2 complex) formation, (2) adsorption of EMIM– CO_2 complex on the reduced carbon atoms, and (3) CO formation. (Reprinted with permission from Ref. [36]. Copyright 2013 SpringerNature).

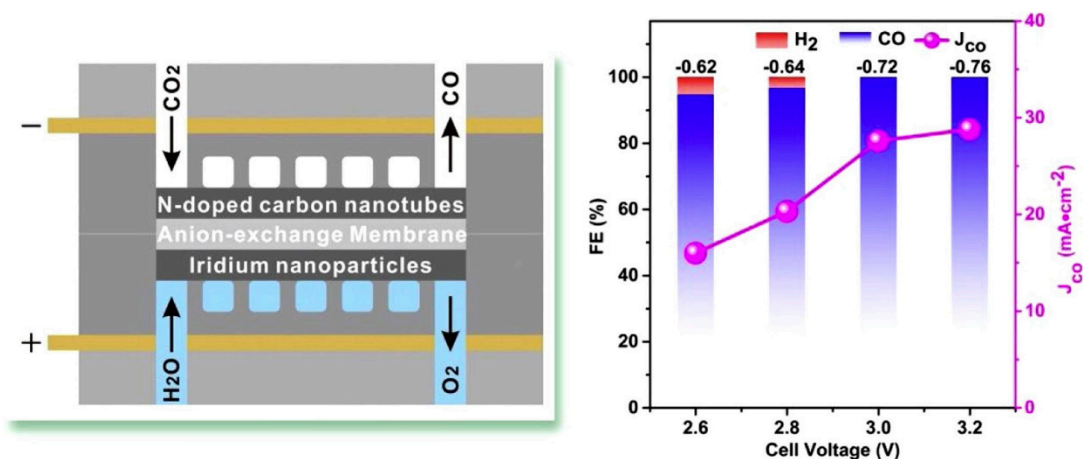


Figure 8. Gas–phase electrolysis in a flow cell and gas-phase CO_2 electrolysis. FE of CO (blue) and H_2 (red) vs. cell voltage (left axis) and partial current density of CO vs. cell voltage (right axis), values above the column are cathode potentials vs. normal hydrogen electrode (NHE) (Reprinted with permission from Ref. [121]. Copyright 2019 Elsevier).

To boost the concentration of pyridine N, phenanthroline was utilized as a precursor [121]. The effects of N doping and atomic configurations on activity were studied, and catalytic active sites were discovered. The mechanism of CO_2RR on NCNTs was also

postulated. By pyrolysis of a phenanthroline heterocycle precursor, nitrogen-doped carbon nanotubes (NCNTs) with a high concentration of pyridinic N sites (62.3 percent) were created, and they can convert CO_2 to CO with great selectivity and stability. Between 0.6 and 0.9 V versus the reversible hydrogen electrode (RHE), the Faradaic efficiency of CO was maintained at >94.5 percent, and the CO current density was as high as -20.2 mA cm^{-2} (Figure 8). Furthermore, after 40 h of electrolysis at -0.8 V , the CO faradic efficiency remained stable at 95% (Figure 8). The remarkable performance was attributed to the large quantities of pyridine N sites in NCNTs, which serve as catalytic active sites. Furthermore, gas-phase CO_2 electrolysis demonstrated approximately 100% Faradic efficiency for CO (Figure 8), implying that the NCNT can optimize CO_2 reduction efficiency while entirely suppressing hydrogen evolution.

Researchers coupled a high inherent defect density acquired by adjusting the size and shape of carbon nanostructures at the nanometer scale with foreign N-doping to create an improved metal-free catalyst for the electroreduction of CO_2 to value-added compounds (Figure 9) [35]. The end product, N-doped graphene quantum dots (NGQDs), has a much higher density of N-doping defects at edge locations. These NGQDs have high activity for electrochemical CO_2 reduction, as evidenced by high reduction current densities at low overpotentials, and, more importantly, they preferentially produce multi-carbon hydrocarbons and oxygenates, particularly the C_2 products ethylene (C_2H_4) and ethanol ($\text{C}_2\text{H}_5\text{OH}$), at FEs comparable to those obtained with Cu nanoparticle-based catalysts.

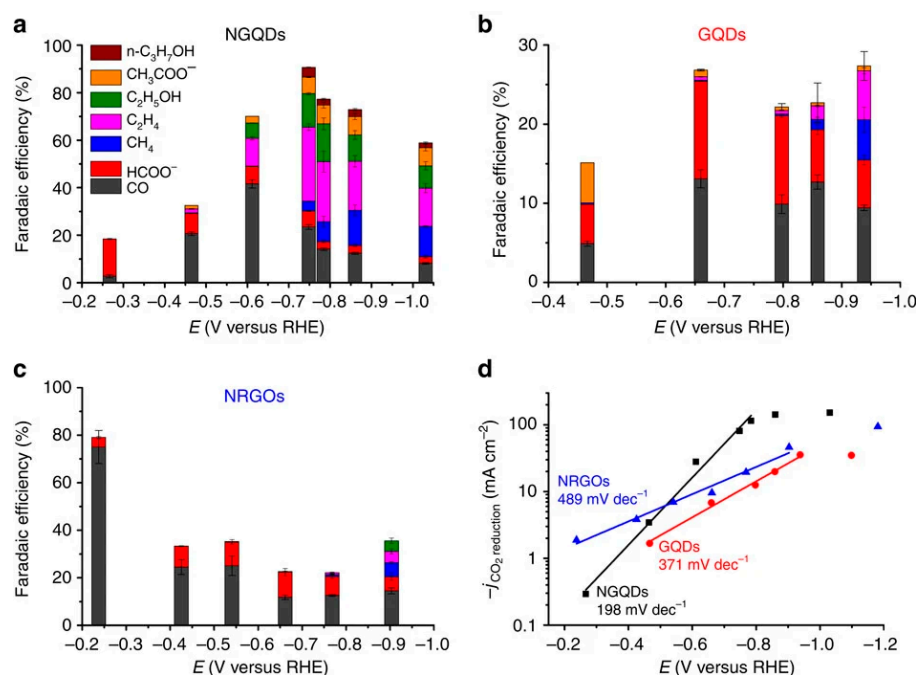


Figure 9. Electrocatalytic activity of carbon nanostructures towards CO_2 reduction. (a) FEs of carbon monoxide (CO), methane (CH_4), ethylene (C_2H_4), formate (HCOO^-), ethanol (EtOH), acetate (AcO^-) and n-propanol (n-PrOH) at various applied cathodic potential for NGQDs. (b) FE of CO_2 reduction products for pristine GQDs. (c) Selectivity to CO_2 reduction products for NRGs. (d) Tafel plots of partial current density of CO_2 reduction versus applied cathodic potential for three nanostructured carbon catalysts. The error bar represents the s.d. of three separate measurements for an electrode. (Reprinted with permission from Ref. [35]. Copyright 2016 SpringerNature).

2.4. Porphyrins, Covalent, and Metal-Organic Framework Catalysts

Porphyrins and other organometallic compounds have long been explored for the CO_2RR and were among the first materials to solve the problems associated with metal electrodes [1,122,123]. In our recent study, we have elucidated the working state of iron porphyrin for the CO_2 -to-CO in an aqueous medium [124]. Using operando UV-

spectroscopy and X-ray absorption near-edge structure spectra, we have confirmed that during the cathodic reaction, the Fe(II) species acts as catalytic sites that accommodate CO as Fe(II)–CO adducts. DFT studies have confirmed and pointed out that the ligand [Fe(II)F₂₀(TPP●)]–prevails in the catalytic cycle prior to the rate-controlling step.

Metal-functionalized porphyrin materials that are employed as CO₂RR electrocatalysts are typically synthesized as homogeneous molecular catalysts. As a consequence, a variety of porphyrins may be functionalized with a variety of transition metal centers (Co, Fe, Zn, Cu, etc.) and the resulting electrocatalysts have well-defined active centers that can be carefully adjusted for high activity and selectivity towards the CO₂RR [1,125–129].

The active centers of heterogeneous electrocatalysts are typically difficult to characterize, making performance optimization difficult. Heterogeneous electrocatalysts, on the other hand, provide stability in electrocatalytic function, particularly in aqueous conditions, which is critical for their practical use. In general, however, these molecular catalysts are unstable and degenerate after just a few catalytic cycles, in addition to catalyst–electrolyte separation difficulties [128]. In order to synergistically boost the stability and effectiveness of homogeneous porphyrin-based catalysts, such as weak Lewis and Brønsted acids, a co-catalyst is usually used in solution with them [130–132]. The production of Fe porphyrin dimers with carefully adjusted Fe center spacing is a new example that addresses some of these challenges [128]. Without the use of co-catalysts, the presence of two metal centers resulted in coordinated stabilization and binding of CO₂ molecules, which boosted activity and stability.

Transition metal porphyrin and other organometallic materials have recently been synthesized and constructed as metal–organic frameworks (MOFs) and covalent organic frameworks (COFs) and functionalized on other nanostructured supports such as graphene and MWCNTs in an effort to combine the exemplary features of both homogeneous and heterogeneous electrocatalysts [125–127,133]. The porphyrin-based materials are typically prepared using solvothermal or hydrothermal methods, and the resulting materials are then placed on conductive substrates to generate CO₂RR electrodes. The structure of the porphyrins and their well-defined active metal centers are preserved since the electrocatalysts are built without high-temperature stages. Deposition on conductive substrates enhances the stability and electron transport to these active sites, resulting in an improved electrocatalytic activity.

Weng et al. [129] describe copper (II)-5,10,15,20-tetrakis (2,6-dihydroxyphenyl) porphyrin (PorCu), a novel copper-porphyrin complex with unique catalytic characteristics for CO₂ reduction in neutral aqueous conditions. For electrochemical CO₂ reduction to hydrocarbons, the PorCu catalyst exhibits great activity and selectivity (methane and ethylene). The catalyst converted CO₂ to hydrocarbons with a Faradaic efficiency of 44 percent at a mass loading of 0.25 mg/cm² and an electrochemical potential of –0.976 V vs. the reversible hydrogen electrode (RHE), significantly inhibiting the other CO₂ reduction routes. Under the same circumstances, an ultrahigh geometric current density of 21 mA/cm² was reached for simultaneous methane and ethylene production, resulting in turnover frequencies (TOFs) of 4.3 methane and 1.8 ethylene molecules. site^{–1} s^{–1}. The built-in hydroxyl groups on the porphyrin ligand, as well as the oxidation state of the Cu center, were both key elements leading to the higher catalytic activity, according to this research.

Iron porphyrin monomers have been reported to catalyze the electrochemical CO₂ reduction to CO in DMF/tetraalkylammonium salts as a supporting electrolyte, with high selectivity at the electro-generated [Fe^I(por)]^{2–} (conventionally described as [Fe⁰(por)]^{2–} species [134] among the non-precious metal-based 2e[–]/2H⁺ coupled CO₂ electrochemical reduction catalysts. These catalysts, on the other hand, degrade after just a few catalytic cycles [135]. The presence of Lewis acids such as Mg²⁺ and Ca²⁺ [132,136], or weak Brønsted acids such as trifluoroethanol and 1-propanol [130], boosts their catalytic efficiency and stability via a push–pull process where the electro-generated electron-rich [Fe⁰(por)]^{2–} increases their catalytic efficiency and stability. The electron-deficient synergist Lewis or Brønsted acid stimulates the breaking of one of the C–O bonds by pushing an electron pair

to the CO₂ molecule [131]. Due to the large local concentration of protons associated with the phenolic hydroxy substituents, modification of the iron tetraphenylporphyrin monomer, FeTPP, with phenolic hydroxy groups at all phenyl group ortho positions improves its activity and stability for CO₂ electro-reduction to CO [137]. Carbon monoxide dehydrogenase (CODH) is a metalloenzyme with a Ni–Fe dinuclear complex at its active core that facilitates the selective conversion of CO₂ to CO [138]. The electrochemical process supported by CODH produces catalytic CO₂ reduction with a very low overpotential [139]. As a result, dinuclear catalysts are excellent candidates for CO₂ reduction catalysis. Naruta groups [128] previously documented the utilization of multiple cofacial porphyrin dimers as ligands for retaining two manganese ions with an appropriate Mn–Mn separation distance (3.7–6.2 Å) to facilitate water oxidation to oxygen or H₂O₂ disproportionation [140]. The utilization of a dimeric combination of two iron ions as bio-inspired catalysts was described for the first time by Naruta team [128]. In a DMF/10 percent H₂O solution, a cofacial iron tetraphenyl porphyrin dimer, *o*-Fe₂DTPP (Figure 10), effectively and selectively catalyzes the electrochemical reduction of CO₂ to CO. The activity of the 1,3-phenylene bridged iron porphyrin dimer (FeTPP) was compared to that of the comparable iron porphyrin monomer (FeTPP) (*m*-Fe₂DTPP). The CVs of *o*-Fe₂DTPP (0.5 mM) in a DMF/10% H₂O solution containing TBAPF₆ (TBAPF₆ = tetra-*n*-butylammonium hexafluorophosphate, 0.1 M) saturated with Ar gas (blue line) or CO₂ gas (red line) are shown in Figure 10b. The detection of a significant catalytic current in the presence of CO₂ gas was the most intriguing discovery, showing electrocatalytic CO₂ reduction enhanced by *o*-Fe₂DTPP. The emergence of the catalytic peak over the Fe⁺–Fe⁺/Fe⁺–Fe⁰ redox couple under Ar at –1.48/–1.46 V vs. NHE (later, all potentials are given against NHE unless otherwise mentioned) shows the beginning of the catalytic process after the Fe⁺–Fe⁰ porphyrin species was electro-generated. Figure 10c depicts the temporal sequence of the products' appearance. Without the catalyst, H₂ is the only product produced with 99 percent Faradic efficiency and a low average current density of –0.1 mA cm^{–2}. In the presence of *o*-Fe₂DTPP, however, a considerable charge, Q = 41.4 C, was burned at an average current density of –1.15 mA cm^{–2} across a 10 h electrolysis process, with the concurrent generation of CO (88 percent Faradic efficiency) and H₂ (12 percent Faradic efficiency). When the quantity of H₂ created during the control experiment is subtracted, the dimer catalyzes the CO₂ reduction to CO with 95% Faradic efficiency. The present density–time profile revealed no reduction over the previous ten hours.

A study describes the electrochemical reduction of CO₂ to CO and methane, as well as trace quantities of HCOOH and methanol, using a simple Co protoporphyrin molecular catalyst immobilized on a pyrolytic graphite (PG) electrode in a completely aqueous electrolyte solution [127]. Previous research utilizing immobilized Co porphyrins or Co phthalocyanines demonstrated that Co-based catalysts might reach a high FE towards CO, which is very sensitive to pH and potential [141–143]. Immobilized Co-based porphyrins are excellent CO₂ reduction electrocatalysts, according to Shen et al. [127], and can produce multi-electron products such as methane and methanol. More importantly, this research highlights the importance of pH in directing catalytic activity and selectivity towards CO and CH₄, particularly in the absence of coordinating anions in the pH range of 1–3. This great sensitivity to pH is explained by a mechanism that emphasizes the critical significance of the first electron transfer in electrochemically activating CO₂. The authors also show how such a CO₂ reduction process occurs in the experiment and how this characteristic might be used to restrict concurrent hydrogen evolution. Furthermore, researchers demonstrate that the catalyst's overpotential and associated turnover frequency (TOF) for CO₂ reduction match favorably with the best molecular porphyrin-based catalyst in the literature [137]. The authors proposed the mechanism of their study in Figure 11a. As a result, the authors believe that these findings could have significant implications for the development of new and improved molecular catalyst electrodes, as well as the formulation of optimized process conditions for efficient electrochemical CO₂ reduction to CO and the reduction of products to a greater degree. Cobalt porphyrins were investigated in order to take advantage of the

frameworks' distinctive features, such as charge carrier mobility due to π - π stacking and the stability afforded by covalent bonding and reticular geometries [140]. When deposited on porous carbon fabric for electrochemical testing, the COFs had a catalytic onset potential of -0.42 V vs. RHE in CO_2 saturated carbonate electrolyte and a maximal activity of -0.67 V vs. RHE, generating CO predominantly at a FE of 90%. With hydrogen evolution being favored at increasingly negative potentials, this strong selectivity for the CO_2 RR begins to decrease.

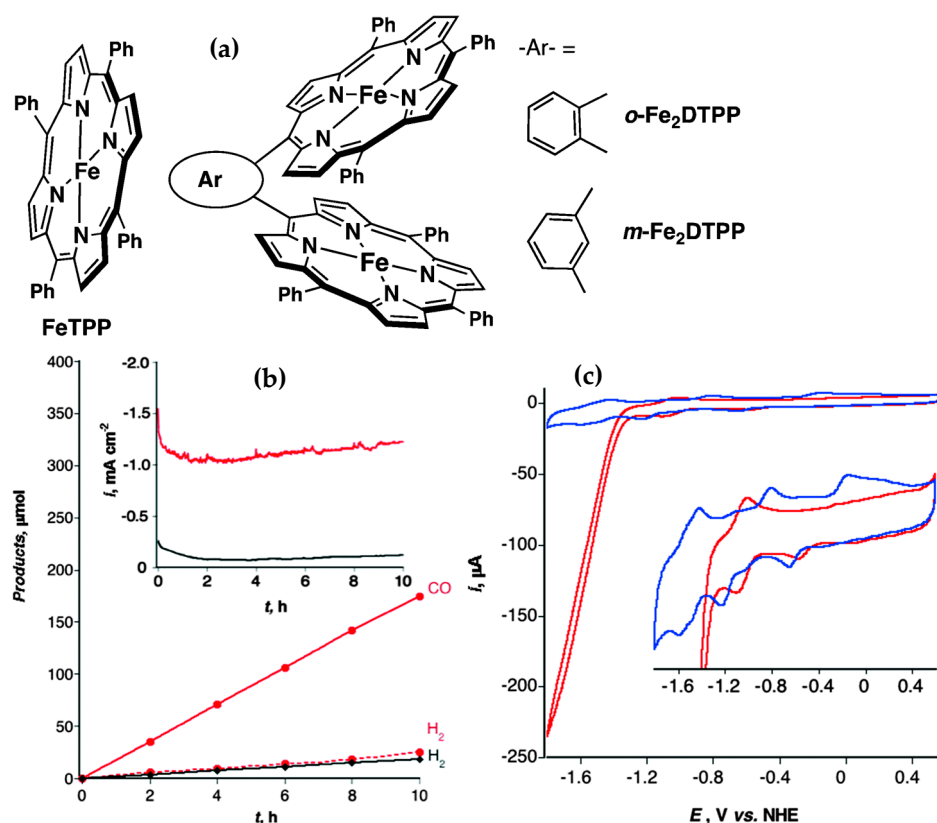


Figure 10. (a) Chemical structures of the iron porphyrin monomer, FeTPP, and iron porphyrin dimers, *o*-Fe₂DTPP and *m*-Fe₂DTPP. (b) CVs of *o*-Fe₂DTPP at 100 mV scan rate in DMF/10% H₂O containing 0.1 M TBAPF₆ supporting electrolyte under Ar or CO₂. Inset: magnified trace of CVs. (c) CO₂ reduction products with time and the current density–time profile (inset) produced during the 10 h chronoamperometry experiment at -1.35 V vs. NHE in a DMF/10% H₂O/0.1 M TBAPF₆ solution saturated with CO₂ without (black lines) and with 0.5 mM *o*-Fe₂DTPP (red lines). (Reprinted with permission from Ref. [128]. Copyright 2015 Royal Society of Chemistry).

COFs were synthesized with longer linkage molecules to increase the spacing between porphyrins for greater pore volume, as illustrated in Figure 1b, in order to improve their performance. As a result, more electrolyte access and CO₂ adsorption were possible, resulting in a lower onset potential (-0.40 V) and a 2.2-fold increase in catalytic activity at -0.67 V. For graphene-enhanced CO₂ diffusion restrictions, as well as Re-porphyrins, were discovered to have a considerable impact on activity [144]. In comparison to non-stirring circumstances, stirring to boost CO₂ diffusion into the electrolyte increased the reaction rate by three times while maintaining selectivity. This is inextricably tied to the fact that, whereas active centers are clearly defined in these materials, active site density is often low, necessitating effective use of active sites.

current density of -10 mA/cm^{-2} at -0.63 V vs. RHE. The carbon black/CoPc and reduced graphene oxide/CoPc showed less than a third of the current density at -0.59 V vs. RHE and a lower FE(CO) as well as low reusability. The authors have yet to improve their performance of the CoPC/CNTs by using the Cyano-substituted CoPc hybrid approach and the prepared catalyst was noted as CoPC-CN/CNT. This substituted catalyst had a current density of -15 mA/cm^{-2} and FE(CO) of 95%. The CNT hybridization acts as a conducting platform, allowing the easiness of electron transfer and enabling the high degree of catalytic site exposure that leads to high current densities. The cyano groups facilitate the electron withdrawal to form the Co^{I} responsible for CO_2 -to-CO reduction.

Copper phthalocyanines (CuPC) have been studied by several groups for their interesting properties for CO_2 reduction properties. Latiff and coworkers [159] have developed a long (10–30 μm) and thin (10–30 nm \varnothing) carbon nanotubes supported by CuPC structures that can efficiently reduce CO_2 with better Faradaic efficiencies. The CuPC/CNTs yielded an overall Faradaic efficiency of 66.3% for C_1 and C_2 byproducts, with CO being the highest evolving product with a Faradaic efficiency of nearly 44% (Figure 12).

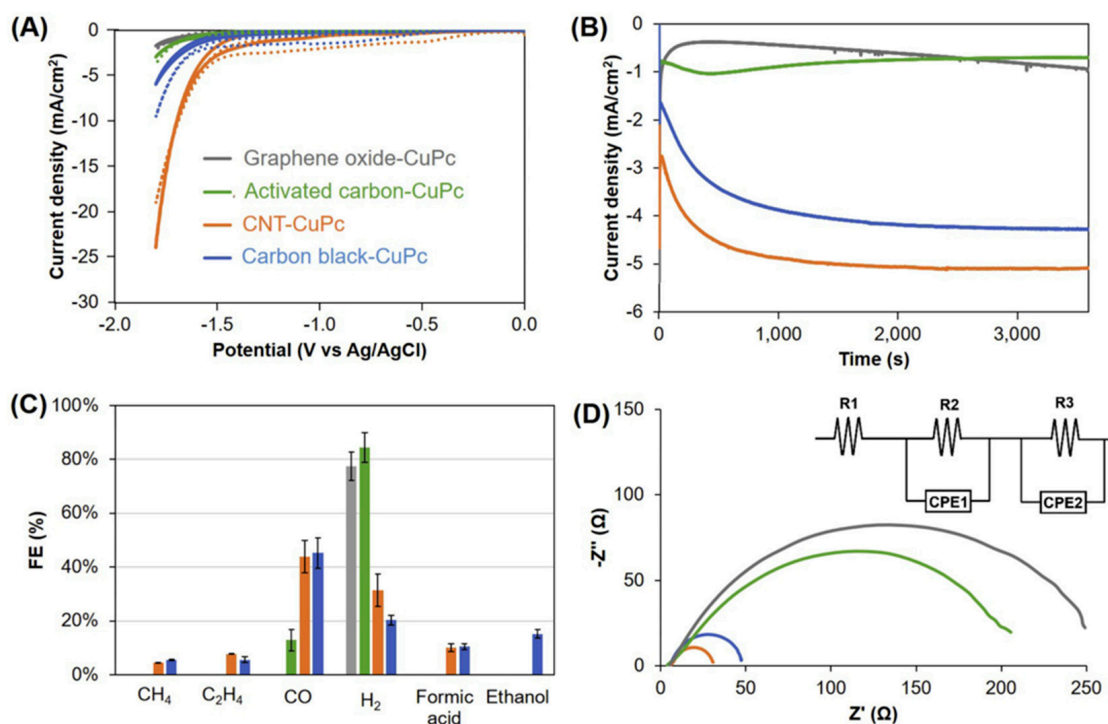


Figure 12. (A) CV measurements of various carbon-supported copper(II) phthalocyanines in CO_2 -saturated (marked in continuous lines) and N_2 -saturated (marked in dotted lines) 0.5 M KCl solution. (B) Chronoamperometry measurements of the materials over 1 h under an applied potential of -1.05 V vs. RHE. (C) Corresponding product analysis results from chronoamperometry runs. (D) EIS spectra for the materials under study are shown by their Nyquist plots, where CPE stands for constant phase element (Reprinted with permission from Ref. [159]. Copyright 2020 Elsevier).

B. Mei et al. have used operando elucidation of the dynamic and structural transformation of CuPc during CO_2 RR electrolysis (Figure 13). Authors have applied operando high-energy resolution fluorescence-detected X-ray absorption spectroscopy to reveal the responsible phenomenon for their observed C_2H_4 formation. They have suggested that the main phenomenon taking place is the aggregation of Cu sites (making copper clusters) with applied potential, leading to the byproduct's formation [160]. Whereas S. Kusama and coworkers reached high electrochemical CO_2 reduction to C_2H_4 with a Faradaic efficiency of 25% by using bare crystalline CuPC supported by a conductive carbon black at -1.6 V vs. Ag/AgCl. The CO and CH_4 were also produced but with low Faradaic efficiency when a limited electrolysis time was performed; however, when long-term 12 h electrolysis

was performed, the CO evolution became more pronounceable, terminating the C_2H_4 evolution [161].

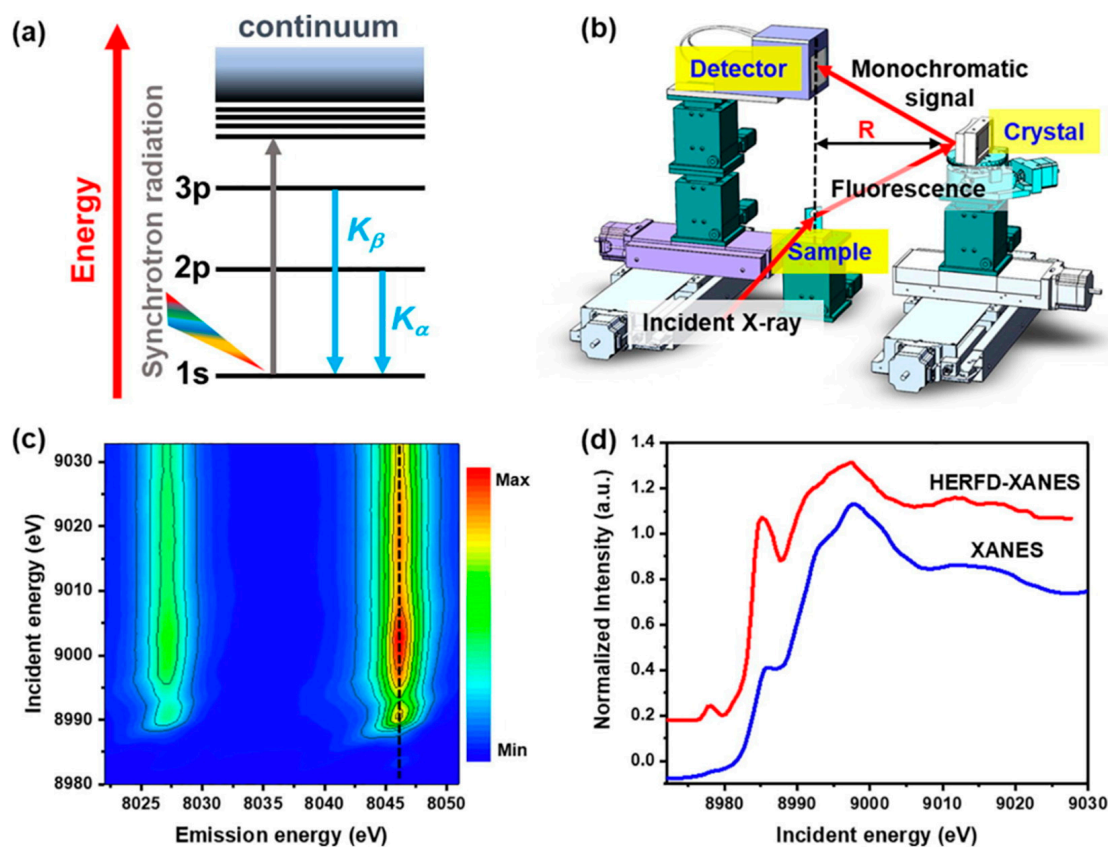


Figure 13. (a) Energy scheme of $K\alpha$ and $K\beta$ emission lines. (b) Experimental setup; (c) $K\alpha$ -RIXS plane of CuO around the Cu K-edge. The contour planes at the emission energy of ~ 8026 and 8046 eV are the $K\alpha_2$ and $K\alpha_1$ -RIXS plane, respectively. The black-dashed line located at constant emission energy of 8046.3 eV. (d) HERFD-XANES (red) and conventional XANES (blue) spectra of CuO (Reprinted with permission from Ref. [160]. Copyright 2022 Elsevier).

Other metal phthalocyanines have also been studied for CO_2 reduction electrolysis, such as tin phthalocyanine [162], nickel phthalocyanines [163], iron phthalocyanines [164], and zinc phthalocyanines [165]. In the case of tin phthalocyanine dichloride, the resulting aggregation hybrid catalyst can catalyze the electroreduction of CO_2 to $HCOOH$ and CO at a total Faradaic efficiency of ca. 90%. The active site of tin phthalocyanine dichloride responsible for electrocatalytic CO_2 reduction is confirmed to be metallic Sn, whose local structure is strongly affected by the adjacent macrocyclic ligands. The dispersed NiPc molecules unlocked remarkable electrocatalytic properties for the CO_2 RR, unlike the aggregated form. The molecular dispersed electrocatalyst NiPc-OMe exhibited FE(CO) of $>99.5\%$ over a wide current density range of -10 to -300 $mA\ cm^{-2}$ and stable performance at the practically relevant current density of -150 $mA\ cm^{-2}$ for 40 h [163].

The iron phthalocyanine electrocatalytic performance of FePc-G, FePc-Gr, FePc-R, FePc-R/ H_2O_2 , FePc/G heterostructures, FePc nanorods, and graphene were investigated to elucidate the role of iron valence degree +II and +III. The optimal catalyst exhibited a high FE(CO) of $>90\%$ at about -0.5 V vs. RHE and an onset potential of -190 mV, and syngas production is easy to obtain and depends mainly on the potential. Furthermore, the DFT simulation revealed that for CO_2 RR, the catalytic activity of Fe(II)Pc should be better than Fe(III)Pc, and that of Fe(II)Pc/Fe(III)Pc dimer higher than individual Fe(II)Pc or Fe(III)Pc [164]. Finally, ZnPc/carbon nitride nanosheet hybrid catalysts could be effectively excited by visible light for PEC- CO_2 RR. The major product was methanol, and the

highest methanol generation efficiency was achieved at -1.0 V. The methanol yield was $13 \mu\text{mol} \cdot \text{L}^{-1}$ after 8 h. The mechanisms for the three different CO_2 RR processes, including PC, EC, and PEC- CO_2 RR, are proposed. In PEC- CO_2 RR, ZnPc/-carbon nitride nanosheets exhibited a synergic effect and methanol production efficiency is much better PC- and EC- CO_2 RR [165].

2.6. CO_2 Reduction Mechanisms

Depending on the three classes of electrocatalysts that were highlighted in the sub-Section 2.1. Different CO_2 value-added products can be obtained. The target byproducts are controlled by tuning the binding energy of the adsorbed intermediate such as (CO^* , COOH^* , CHO^* , COH^*) (Figure 14). For example, when the interaction between the surface of the electrocatalysts and the reduction intermediates is not strong enough, CO and formate are the main reduction products (Type 1 and 2). Inversely, when the electrocatalysts bind strongly with CO^* , this will be further reduced to other by-products (Type 3) [166]. This is where copper shows an incredible ability to transform CO_2 into hydrocarbons, The basic explanation for its ability to generate products other than CO is that Cu binds $^*\text{CO}$ neither too weakly nor too strongly [37].

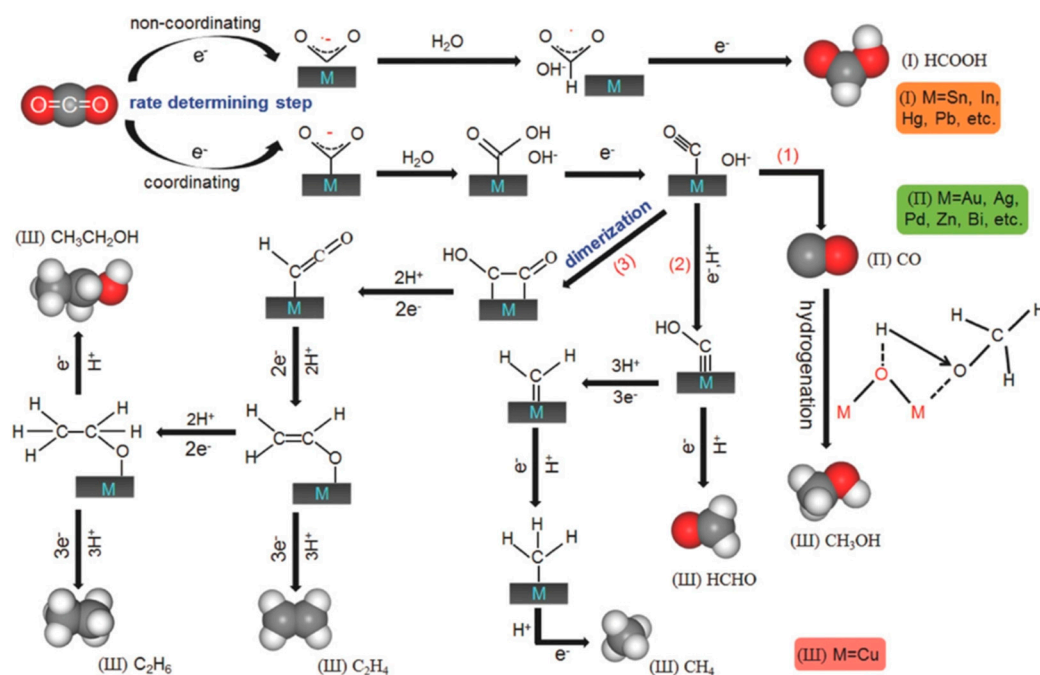


Figure 14. Schematic mechanism of different metal electrocatalysts for CO_2 reduction reaction in aqueous solution. (Reprinted with permission from Ref. [165]. Copyright 2019 Elsevier).

3. Conclusions and Prospects

The Electrochemical CO_2 reduction technique is still in its early stages compared to other CO_2 conversion technologies, although it is being actively researched. For electrochemical CO_2 reduction, a range of materials have been investigated as catalysts, and the catalysts should be modified depending on the intended products. Nanostructured catalysts should be further adjusted in light of the cell design of gas-diffusion electrodes. To date, the majority of investigations have employed pure CO_2 that has been concentrated; however, for practical applications, the conversion of dilute CO_2 , especially in the presence of possible catalyst poisons such as S compounds, should be researched more intensively. In addition, several technological hurdles remain in CO_2 electrochemical reduction technology, including (i) inadequate catalyst activity, (ii) limited product selectivity, and (iii) insufficient stability. Our technology appears to be far from adequate when it comes to the actual application of CO_2 reduction to creating useable low-carbon fuels. Low catalyst stability

appears to be the current key barrier to industrial-scale deployment. As a result, the main emphasis of effort in this field remains the development of highly active, selective, and stable electrocatalysts for CO₂ reduction.

Author Contributions: H.A.A.: Conceptualization; Writing the draft, Data curation; Formal analysis; Project administration. M.Z.: Writing the draft, review & editing; Data curation; Formal analysis. A.B.: Writing—review & editing. M.A.: Writing—review & editing. All authors have read and agreed to the published version of the manuscript.

Funding: This research received no external funding.

Acknowledgments: This work was supported by the faculty of sciences and the Mohammed V University in Rabat.

Conflicts of Interest: The authors declare no conflict of interest.

References

1. Qiao, J.; Liu, Y.; Hong, F.; Zhang, J. A review of catalysts for the electroreduction of carbon dioxide to produce low-carbon fuels. *Chem. Soc. Rev.* **2014**, *43*, 631–675. [[CrossRef](#)] [[PubMed](#)]
2. Dincer, I. Renewable energy and sustainable development: A crucial review. *Renew. Sustain. Energy Rev.* **2000**, *4*, 157–175. [[CrossRef](#)]
3. Burke, M.J.; Stephens, J.C. Political power and renewable energy futures: A critical review. *Energy Res. Soc. Sci.* **2018**, *35*, 78–93. [[CrossRef](#)]
4. Álvarez, A.; Bansode, A.; Urakawa, A.; Bavykina, A.V.; Wezendonk, T.A.; Makkee, M.; Gascon, J.; Kapteijn, F. Challenges in the Greener Production of Formates/Formic Acid, Methanol, and DME by Heterogeneously Catalyzed CO₂ Hydrogenation Processes. *Chem. Rev.* **2017**, *117*, 9804–9838. [[CrossRef](#)] [[PubMed](#)]
5. Zhang, Y.; Su, X.; Li, L.; Qi, H.; Yang, C.; Liu, W.; Pan, X.; Liu, X.; Yang, X.; Huang, Y.; et al. Ru/TiO₂ catalysts with size-dependent metal/support interaction for tunable reactivity in Fischer-Tropsch synthesis. *ACS Catal.* **2020**, *10*, 12967–12975. [[CrossRef](#)]
6. Kang, J.; He, S.; Zhou, W.; Shen, Z.; Li, Y.; Chen, M.; Zhang, Q.; Wang, Y. Single-pass transformation of syngas into ethanol with high selectivity by triple tandem catalysis. *Nat. Commun.* **2020**, *11*, 827. [[CrossRef](#)]
7. Wang, W.-H.; Himeda, Y.; Muckerman, J.T.; Manbeck, G.F.; Fujita, E. CO₂ Hydrogenation to Formate and Methanol as an Alternative to Photo- and Electrochemical CO₂ Reduction. *Chem. Rev.* **2015**, *115*, 12936–12973. [[CrossRef](#)]
8. Li, W.; Wang, H.; Jiang, X.; Zhu, J.; Liu, Z.; Guo, X.; Song, C. A short review of recent advances in CO₂ hydrogenation to hydrocarbons over heterogeneous catalysts. *RSC Adv.* **2018**, *8*, 7651–7669. [[CrossRef](#)]
9. Albo, J.; Alvarez-Guerra, M.; Castaño, P.; Irabien, A. Towards the electrochemical conversion of carbon dioxide into methanol. *Green Chem.* **2015**, *17*, 2304–2324. [[CrossRef](#)]
10. Olah, G.A. Beyond Oil and Gas: The Methanol Economy. *Angew. Chemie Int. Ed.* **2005**, *44*, 2636–2639. [[CrossRef](#)]
11. Albo, J.; Sáez, A.; Solla-Gullón, J.; Montiel, V.; Irabien, A. Production of methanol from CO₂ electroreduction at Cu₂O and Cu₂O/ZnO-based electrodes in aqueous solution. *Appl. Catal. B Environ.* **2015**, *176–177*, 709–717. [[CrossRef](#)]
12. Alvarez-Guerra, M.; Quintanilla, S.; Irabien, A. Conversion of carbon dioxide into formate using a continuous electrochemical reduction process in a lead cathode. *Chem. Eng. J.* **2012**, *207*, 278–284. [[CrossRef](#)]
13. Del Castillo, A.; Alvarez-Guerra, M.; Irabien, A. Continuous electroreduction of CO₂ to formate using Sn gas diffusion electrodes. *AIChE J.* **2014**, *60*, 3557–3564. [[CrossRef](#)]
14. Wang, Q.; Dong, H.; Yu, H. Fabrication of a novel tin gas diffusion electrode for electrochemical reduction of carbon dioxide to formic acid. *RSC Adv.* **2014**, *4*, 59970–59976. [[CrossRef](#)]
15. Wang, Q.; Dong, H.; Yu, H. Development of rolling tin gas diffusion electrode for carbon dioxide electrochemical reduction to produce formate in aqueous electrolyte. *J. Power Sources* **2014**, *271*, 278–284. [[CrossRef](#)]
16. Jhong, H.-R. “Molly”; Brushett, F.R.; Kenis, P.J.A. The Effects of Catalyst Layer Deposition Methodology on Electrode Performance. *Adv. Energy Mater.* **2013**, *3*, 589–599. [[CrossRef](#)]
17. Vass, A.; Endrődi, B.; Samu, G.F.; Balog, A.; Kormányos, A.; Cherevko, S.; Janáky, C. Local Chemical Environment Governs Anode Processes in CO₂ Electrolyzers. *ACS Energy Lett.* **2021**, *6*, 3801–3808. [[CrossRef](#)]
18. Vass, A.; Kormányos, A.; Kószó, Z.; Endrődi, B.; Janáky, C. Anode Catalysts in CO₂ Electrolysis: Challenges and Untapped Opportunities. *ACS Catal.* **2022**, *12*, 1037–1051. [[CrossRef](#)]
19. Zhu, D.D.; Liu, J.L.; Qiao, S.Z. Recent Advances in Inorganic Heterogeneous Electrocatalysts for Reduction of Carbon Dioxide. *Adv. Mater.* **2016**, *28*, 3423–3452. [[CrossRef](#)]
20. Zhang, L.; Zhao, Z.-J.; Gong, J. Nanostructured Materials for Heterogeneous Electrocatalytic CO₂ Reduction and their Related Reaction Mechanisms. *Angew. Chem. Int. Ed.* **2017**, *56*, 11326–11353. [[CrossRef](#)]
21. Vasileff, A.; Zheng, Y.; Qiao, S.Z. Carbon Solving Carbon’s Problems: Recent Progress of Nanostructured Carbon-Based Catalysts for the Electrochemical Reduction of CO₂. *Adv. Energy Mater.* **2017**, *7*, 1700759. [[CrossRef](#)]

22. Lu, Q.; Rosen, J.; Zhou, Y.; Hutchings, G.S.; Kimmel, Y.C.; Chen, J.G.; Jiao, F. A selective and efficient electrocatalyst for carbon dioxide reduction. *Nat. Commun.* **2014**, *5*, 3242. [[CrossRef](#)] [[PubMed](#)]
23. Zhu, W.; Zhang, Y.-J.; Zhang, H.; Lv, H.; Li, Q.; Michalsky, R.; Peterson, A.A.; Sun, S. Active and Selective Conversion of CO₂ to CO on Ultrathin Au Nanowires. *J. Am. Chem. Soc.* **2014**, *136*, 16132–16135. [[CrossRef](#)]
24. Kim, C.; Jeon, H.S.; Eom, T.; Jee, M.S.; Kim, H.; Friend, C.M.; Min, B.K.; Hwang, Y.J. Achieving Selective and Efficient Electrocatalytic Activity for CO₂ Reduction Using Immobilized Silver Nanoparticles. *J. Am. Chem. Soc.* **2015**, *137*, 13844–13850. [[CrossRef](#)] [[PubMed](#)]
25. Sun, K.; Cheng, T.; Wu, L.; Hu, Y.; Zhou, J.; Maclennan, A.; Jiang, Z.; Gao, Y.; Goddard, W.A.; Wang, Z. Ultrahigh Mass Activity for Carbon Dioxide Reduction Enabled by Gold–Iron Core–Shell Nanoparticles. *J. Am. Chem. Soc.* **2017**, *139*, 15608–15611. [[CrossRef](#)] [[PubMed](#)]
26. Chen, Y.; Kanan, M.W. Tin Oxide Dependence of the CO₂ Reduction Efficiency on Tin Electrodes and Enhanced Activity for Tin/Tin Oxide Thin-Film Catalysts. *J. Am. Chem. Soc.* **2012**, *134*, 1986–1989. [[CrossRef](#)] [[PubMed](#)]
27. Zhang, S.; Kang, P.; Meyer, T.J. Nanostructured Tin Catalysts for Selective Electrochemical Reduction of Carbon Dioxide to Formate. *J. Am. Chem. Soc.* **2014**, *136*, 1734–1737. [[CrossRef](#)]
28. Fan, L.; Xia, Z.; Xu, M.; Lu, Y.; Li, Z. 1D SnO₂ with Wire-in-Tube Architectures for Highly Selective Electrochemical Reduction of CO₂ to C₁ Products. *Adv. Funct. Mater.* **2018**, *28*, 1706289. [[CrossRef](#)]
29. Duan, Y.-X.; Meng, F.-L.; Liu, K.-H.; Yi, S.-S.; Li, S.-J.; Yan, J.-M.; Jiang, Q. Amorphizing of Cu Nanoparticles toward Highly Efficient and Robust Electrocatalyst for CO₂ Reduction to Liquid Fuels with High Faradaic Efficiencies. *Adv. Mater.* **2018**, *30*, 1706194. [[CrossRef](#)]
30. Li, C.W.; Kanan, M.W. CO₂ Reduction at Low Overpotential on Cu Electrodes Resulting from the Reduction of Thick Cu₂O Films. *J. Am. Chem. Soc.* **2012**, *134*, 7231–7234. [[CrossRef](#)]
31. Gao, S.; Jiao, X.; Sun, Z.; Zhang, W.; Sun, Y.; Wang, C.; Hu, Q.; Zu, X.; Yang, F.; Yang, S.; et al. Ultrathin Co₃O₄ Layers Realizing Optimized CO₂ Electroreduction to Formate. *Angew. Chemie Int. Ed.* **2016**, *55*, 698–702. [[CrossRef](#)] [[PubMed](#)]
32. Gao, S.; Lin, Y.; Jiao, X.; Sun, Y.; Luo, Q.; Zhang, W.; Li, D.; Yang, J.; Xie, Y. Partially oxidized atomic cobalt layers for carbon dioxide electroreduction to liquid fuel. *Nature* **2016**, *529*, 68–71. [[CrossRef](#)] [[PubMed](#)]
33. Pan, Y.; Lin, R.; Chen, Y.; Liu, S.; Zhu, W.; Cao, X.; Chen, W.; Wu, K.; Cheong, W.-C.; Wang, Y.; et al. Design of Single-Atom Co–N₅ Catalytic Site: A Robust Electrocatalyst for CO₂ Reduction with Nearly 100% CO Selectivity and Remarkable Stability. *J. Am. Chem. Soc.* **2018**, *140*, 4218–4221. [[CrossRef](#)] [[PubMed](#)]
34. Song, Y.; Chen, W.; Zhao, C.; Li, S.; Wei, W.; Sun, Y. Metal-Free Nitrogen-Doped Mesoporous Carbon for Electroreduction of CO₂ to Ethanol. *Angew. Chemie* **2017**, *129*, 10980–10984. [[CrossRef](#)]
35. Wu, J.; Ma, S.; Sun, J.; Gold, J.I.; Tiwary, C.; Kim, B.; Zhu, L.; Chopra, N.; Odeh, I.N.; Vajtai, R.; et al. A metal-free electrocatalyst for carbon dioxide reduction to multi-carbon hydrocarbons and oxygenates. *Nat. Commun.* **2016**, *7*, 13869. [[CrossRef](#)] [[PubMed](#)]
36. Kumar, B.; Asadi, M.; Pisasale, D.; Sinha-Ray, S.; Rosen, B.A.; Haasch, R.; Abiade, J.; Yarin, A.L.; Salehi-Khojin, A. Renewable and metal-free carbon nanofibre catalysts for carbon dioxide reduction. *Nat. Commun.* **2013**, *4*, 2819. [[CrossRef](#)]
37. Vasileff, A.; Xu, C.; Jiao, Y.; Zheng, Y.; Qiao, S.-Z. Surface and Interface Engineering in Copper-Based Bimetallic Materials for Selective CO₂ Electroreduction. *Chem* **2018**, *4*, 1809–1831. [[CrossRef](#)]
38. Wang, Y.; Liu, J.; Wang, Y.; Al-Enizi, A.M.; Zheng, G. Tuning of CO₂ Reduction Selectivity on Metal Electrocatalysts. *Small* **2017**, *13*, 1701809. [[CrossRef](#)]
39. Feaster, J.T.; Shi, C.; Cave, E.R.; Hatsukade, T.; Abram, D.N.; Kuhl, K.P.; Hahn, C.; Nørskov, J.K.; Jaramillo, T.F. Understanding Selectivity for the Electrochemical Reduction of Carbon Dioxide to Formic Acid and Carbon Monoxide on Metal Electrodes. *ACS Catal.* **2017**, *7*, 4822–4827. [[CrossRef](#)]
40. Hatsukade, T.; Kuhl, K.P.; Cave, E.R.; Abram, D.N.; Jaramillo, T.F. Insights into the electrocatalytic reduction of CO₂ on metallic silver surfaces. *Phys. Chem. Chem. Phys.* **2014**, *16*, 13814–13819. [[CrossRef](#)]
41. Zhang, B.; Zhang, B.; Jiang, Y.; Ma, T.; Pan, H.; Sun, W. Single-atom electrocatalysts for multi-electron reduction of CO₂. *Small* **2021**, *17*, 2101443. [[CrossRef](#)] [[PubMed](#)]
42. Zhu, S.; Delmo, E.P.; Li, T.; Qin, X.; Tian, J.; Zhang, L.; Shao, M. Recent advances in catalyst structure and composition engineering strategies for regulating CO₂ electrochemical reduction. *Adv. Mater.* **2021**, *33*, 2005484. [[CrossRef](#)] [[PubMed](#)]
43. Jhong, H.R.; Nwabara, U.O.; Shubert-Zuleta, S.; Grundish, N.S.; Tandon, B.; Reimnitz, L.C.; Staller, C.M.; Ong, G.K.; Cabezas, C.A.S.; Goodenough, J.B.; et al. Efficient Aqueous Electroreduction of CO₂ to Formate at Low Overpotential on Indium Tin Oxide Nanocrystals. *Chem. Mater.* **2021**, *33*, 7675–7685. [[CrossRef](#)]
44. Wei, F.; Wang, T.; Jiang, X.; Ai, Y.; Cui, A.; Cui, J.; Fu, J.; Cheng, J.; Lei, L.; Hou, Y.; et al. Controllably engineering mesoporous surface and dimensionality of SnO₂ toward high-performance CO₂ electroreduction. *Adv. Funct. Mater.* **2020**, *30*, 2002092. [[CrossRef](#)]
45. Hailu, A.; Tamijani, A.A.; Mason, S.E.; Shaw, S.K. Efficient conversion of CO₂ to formate using inexpensive and easily prepared post-transition metal alloy catalysts. *Energ. Fuel.* **2020**, *34*, 3467–3476. [[CrossRef](#)]
46. Li, Z.; Feng, Y.; Li, Y.; Chen, X.; Li, N.; He, W.; Liu, J. Fabrication of Bi/Sn bimetallic electrode for high-performance electrochemical reduction of carbon dioxide to formate. *Chem. Eng. J.* **2022**, *428*, 130901. [[CrossRef](#)]
47. Wen, J.; Wan, Z.; Hu, X.; Huang, J.; Kang, X. Restructuring of copper catalysts by potential cycling and enhanced two-carbon production for electroreduction of carbon dioxide. *J. CO₂ Util.* **2022**, *56*, 101846. [[CrossRef](#)]

48. Lee, H.-E.; Yang, K.D.; Yoon, S.M.; Ahn, H.-Y.; Lee, Y.Y.; Chang, H.; Jeong, D.H.; Lee, Y.-S.; Kim, M.Y.; Nam, K.T. Concave Rhombic Dodecahedral Au Nanocatalyst with Multiple High-Index Facets for CO₂ Reduction. *ACS Nano* **2015**, *9*, 8384–8393. [[CrossRef](#)]
49. Kim, J.-H.; Woo, H.; Choi, J.; Jung, H.-W.; Kim, Y.-T. CO₂ Electroreduction on Au/TiC: Enhanced Activity Due to Metal–Support Interaction. *ACS Catal.* **2017**, *7*, 2101–2106. [[CrossRef](#)]
50. Won, D.H.; Shin, H.; Koh, J.; Chung, J.; Lee, H.S.; Kim, H.; Woo, S.I. Highly Efficient, Selective, and Stable CO₂ Electroreduction on a Hexagonal Zn Catalyst. *Angew. Chemie Int. Ed.* **2016**, *55*, 9297–9300. [[CrossRef](#)]
51. Rosen, J.; Hutchings, G.S.; Lu, Q.; Forest, R.V.; Moore, A.; Jiao, F. Electrodeposited Zn Dendrites with Enhanced CO Selectivity for Electrocatalytic CO₂ Reduction. *ACS Catal.* **2015**, *5*, 4586–4591. [[CrossRef](#)]
52. Cho, M.; Song, J.T.; Back, S.; Jung, Y.; Oh, J. The Role of Adsorbed CN and Cl on an Au Electrode for Electrochemical CO₂ Reduction. *ACS Catal.* **2018**, *8*, 1178–1185. [[CrossRef](#)]
53. Jiang, K.; Kharel, P.; Peng, Y.; Gangishetty, M.K.; Lin, H.-Y.G.; Stavitski, E.; Attenkofer, K.; Wang, H. Silver Nanoparticles with Surface-Bonded Oxygen for Highly Selective CO₂ Reduction. *ACS Sustain. Chem. Eng.* **2017**, *5*, 8529–8534. [[CrossRef](#)]
54. Nursanto, E.B.; Jeon, H.S.; Kim, C.; Jee, M.S.; Koh, J.H.; Hwang, Y.J.; Min, B.K. Gold catalyst reactivity for CO₂ electro-reduction: From nano particle to layer. *Catal. Today* **2016**, *260*, 107–111. [[CrossRef](#)]
55. Verma, S.; Hamasaki, Y.; Kim, C.; Huang, W.; Lu, S.; Jhong, H.-R.M.; Gewirth, A.A.; Fujigaya, T.; Nakashima, N.; Kenis, P.J.A. Insights into the Low Overpotential Electroreduction of CO₂ to CO on a Supported Gold Catalyst in an Alkaline Flow Electrolyzer. *ACS Energy Lett.* **2018**, *3*, 193–198. [[CrossRef](#)]
56. Mistry, H.; Reske, R.; Zeng, Z.; Zhao, Z.-J.; Greeley, J.; Strasser, P.; Cuenya, B.R. Exceptional Size-Dependent Activity Enhancement in the Electroreduction of CO₂ over Au Nanoparticles. *J. Am. Chem. Soc.* **2014**, *136*, 16473–16476. [[CrossRef](#)]
57. Yoon, Y.; Hall, A.S.; Surendranath, Y. Tuning of Silver Catalyst Mesostructure Promotes Selective Carbon Dioxide Conversion into Fuels. *Angew. Chemie Int. Ed.* **2016**, *55*, 15282–15286. [[CrossRef](#)]
58. Hall, A.S.; Yoon, Y.; Wuttig, A.; Surendranath, Y. Mesostructure-Induced Selectivity in CO₂ Reduction Catalysis. *J. Am. Chem. Soc.* **2015**, *137*, 14834–14837. [[CrossRef](#)]
59. Mariano, R.G.; Kang, M.; Wahab, O.J.; McPherson, I.J.; Rabinowitz, J.A.; Unwin, P.R.; Kanan, M.W. Microstructural origin of locally enhanced CO₂ electroreduction activity on gold. *Nat. Mater.* **2021**, *20*, 1000–1006. [[CrossRef](#)]
60. Christophe, J.; Doneux, T.; Buess-Herman, C. Electroreduction of Carbon Dioxide on Copper-Based Electrodes: Activity of Copper Single Crystals and Copper–Gold Alloys. *Electrocatalysis* **2012**, *3*, 139–146. [[CrossRef](#)]
61. Jia, F.; Yu, X.; Zhang, L. Enhanced selectivity for the electrochemical reduction of CO₂ to alcohols in aqueous solution with nanostructured Cu–Au alloy as catalyst. *J. Power Sources* **2014**, *252*, 85–89. [[CrossRef](#)]
62. Kim, D.; Resasco, J.; Yu, Y.; Asiri, A.M.; Yang, P. Synergistic geometric and electronic effects for electrochemical reduction of carbon dioxide using gold–copper bimetallic nanoparticles. *Nat. Commun.* **2014**, *5*, 4948. [[CrossRef](#)] [[PubMed](#)]
63. Kim, D.; Xie, C.; Becknell, N.; Yu, Y.; Karamad, M.; Chan, K.; Crumlin, E.J.; Nørskov, J.K.; Yang, P. Electrochemical Activation of CO₂ through Atomic Ordering Transformations of AuCu Nanoparticles. *J. Am. Chem. Soc.* **2017**, *139*, 8329–8336. [[CrossRef](#)] [[PubMed](#)]
64. Ross, M.B.; Dinh, C.T.; Li, Y.; Kim, D.; De Luna, P.; Sargent, E.H.; Yang, P. Tunable Cu Enrichment Enables Designer Syngas Electrosynthesis from CO₂. *J. Am. Chem. Soc.* **2017**, *139*, 9359–9363. [[CrossRef](#)] [[PubMed](#)]
65. Monzó, J.; Malewski, Y.; Kortlever, R.; Vidal-Iglesias, F.J.; Solla-Gullón, J.; Koper, M.T.M.; Rodriguez, P. Enhanced electrocatalytic activity of Au@Cu core@shell nanoparticles towards CO₂ reduction. *J. Mater. Chem. A* **2015**, *3*, 23690–23698. [[CrossRef](#)]
66. Shi, C.; Hansen, H.A.; Lausche, A.C.; Nørskov, J.K. Trends in electrochemical CO₂ reduction activity for open and close-packed metal surfaces. *Phys. Chem. Chem. Phys.* **2014**, *16*, 4720. [[CrossRef](#)]
67. Chen, K.; Zhang, X.; Williams, T.; Bourgeois, L.; MacFarlane, D.R. Electrochemical reduction of CO₂ on core-shell Cu/Au nanostructure arrays for syngas production. *Electrochim. Acta* **2017**, *239*, 84–89. [[CrossRef](#)]
68. Pander, J.E.; Ren, D.; Huang, Y.; Loo, N.W.X.; Hong, S.H.L.; Yeo, B.S. Understanding the Heterogeneous Electrocatalytic Reduction of Carbon Dioxide on Oxide-Derived Catalysts. *ChemElectroChem* **2018**, *5*, 219–237. [[CrossRef](#)]
69. Ren, D.; Deng, Y.; Handoko, A.D.; Chen, C.S.; Malkhandi, S.; Yeo, B.S. Selective Electrochemical Reduction of Carbon Dioxide to Ethylene and Ethanol on Copper(I) Oxide Catalysts. *ACS Catal.* **2015**, *5*, 2814–2821. [[CrossRef](#)]
70. Lee, S.Y.; Jung, H.; Kim, N.-K.; Oh, H.-S.; Min, B.K.; Hwang, Y.J. Mixed Copper States in Anodized Cu Electrocatalyst for Stable and Selective Ethylene Production from CO₂ Reduction. *J. Am. Chem. Soc.* **2018**, *140*, 8681–8689. [[CrossRef](#)]
71. Lee, S.; Kim, D.; Lee, J. Electrocatalytic Production of C₃–C₄ Compounds by Conversion of CO₂ on a Chloride-Induced Bi-Phasic Cu₂O–Cu Catalyst. *Angew. Chemie Int. Ed.* **2015**, *54*, 14701–14705. [[CrossRef](#)] [[PubMed](#)]
72. Won, D.H.; Choi, C.H.; Chung, J.; Chung, M.W.; Kim, E.-H.; Woo, S.I. Rational Design of a Hierarchical Tin Dendrite Electrode for Efficient Electrochemical Reduction of CO₂. *ChemSusChem* **2015**, *8*, 3092–3098. [[CrossRef](#)] [[PubMed](#)]
73. Chen, Y.; Li, C.W.; Kanan, M.W. Aqueous CO₂ Reduction at Very Low Overpotential on Oxide-Derived Au Nanoparticles. *J. Am. Chem. Soc.* **2012**, *134*, 19969–19972. [[CrossRef](#)] [[PubMed](#)]
74. Ma, M.; Trzeźniewski, B.J.; Xie, J.; Smith, W.A. Selective and Efficient Reduction of Carbon Dioxide to Carbon Monoxide on Oxide-Derived Nanostructured Silver Electrocatalysts. *Angew. Chem. Int. Ed.* **2016**, *55*, 9748–9752. [[CrossRef](#)]
75. Verdager-Casadevall, A.; Li, C.W.; Johansson, T.P.; Scott, S.B.; McKeown, J.T.; Kumar, M.; Stephens, I.E.L.; Kanan, M.W.; Chorkendorff, I. Probing the Active Surface Sites for CO Reduction on Oxide-Derived Copper Electrocatalysts. *J. Am. Chem. Soc.* **2015**, *137*, 9808–9811. [[CrossRef](#)]

76. Feng, X.; Jiang, K.; Fan, S.; Kanan, M.W. A Direct Grain-Boundary-Activity Correlation for CO Electroreduction on Cu Nanoparticles. *ACS Cent. Sci.* **2016**, *2*, 169–174. [[CrossRef](#)]
77. Kas, R.; Kortlever, R.; Milbrat, A.; Koper, M.T.M.; Mul, G.; Baltrusaitis, J. Electrochemical CO₂ reduction on Cu₂O-derived copper nanoparticles: Controlling the catalytic selectivity of hydrocarbons. *Phys. Chem. Chem. Phys.* **2014**, *16*, 12194–12201. [[CrossRef](#)]
78. Mariano, R.G.; McKelvey, K.; White, H.S.; Kanan, M.W. Selective increase in CO₂ electroreduction activity at grain-boundary surface terminations. *Science* **2017**, *358*, 1187–1192. [[CrossRef](#)]
79. Eilert, A.; Cavalca, F.; Roberts, F.S.; Osterwalder, J.; Liu, C.; Favaro, M.; Crumlin, E.J.; Ogasawara, H.; Friebel, D.; Pettersson, L.G.M.; et al. Subsurface Oxygen in Oxide-Derived Copper Electrocatalysts for Carbon Dioxide Reduction. *J. Phys. Chem. Lett.* **2017**, *8*, 285–290. [[CrossRef](#)]
80. Favaro, M.; Xiao, H.; Cheng, T.; Goddard, W.A.; Yano, J.; Crumlin, E.J. Subsurface oxide plays a critical role in CO₂ activation by Cu(111) surfaces to form chemisorbed CO₂, the first step in reduction of CO₂. *Proc. Natl. Acad. Sci. USA* **2017**, *114*, 6706–6711. [[CrossRef](#)]
81. Lum, Y.; Ager, J.W. Stability of Residual Oxides in Oxide-Derived Copper Catalysts for Electrochemical CO₂ Reduction Investigated with 18 O Labeling. *Angew. Chemie Int. Ed.* **2018**, *57*, 551–554. [[CrossRef](#)] [[PubMed](#)]
82. Albo, J.; Irabien, A. Cu₂O-loaded gas diffusion electrodes for the continuous electrochemical reduction of CO₂ to methanol. *J. Catal.* **2016**, *343*, 232–239. [[CrossRef](#)]
83. Kim, J.; Kim, H.-E.; Lee, H. Single-Atom Catalysts of Precious Metals for Electrochemical Reactions. *ChemSusChem* **2018**, *11*, 104–113. [[CrossRef](#)] [[PubMed](#)]
84. Yang, H.B.; Hung, S.-F.; Liu, S.; Yuan, K.; Miao, S.; Zhang, L.; Huang, X.; Wang, H.-Y.; Cai, W.; Chen, R.; et al. Atomically dispersed Ni(i) as the active site for electrochemical CO₂ reduction. *Nat. Energy* **2018**, *3*, 140–147. [[CrossRef](#)]
85. Jiang, K.; Siahrostami, S.; Zheng, T.; Hu, Y.; Hwang, S.; Stavitski, E.; Peng, Y.; Dynes, J.; Gangisetty, M.; Su, D.; et al. Isolated Ni single atoms in graphene nanosheets for high-performance CO₂ reduction. *Energy Environ. Sci.* **2018**, *11*, 893–903. [[CrossRef](#)]
86. Jiang, K.; Siahrostami, S.; Akey, A.J.; Li, Y.; Lu, Z.; Lattimer, J.; Hu, Y.; Stokes, C.; Gangishetty, M.; Chen, G.; et al. Transition-Metal Single Atoms in a Graphene Shell as Active Centers for Highly Efficient Artificial Photosynthesis. *Chem* **2017**, *3*, 950–960. [[CrossRef](#)]
87. Wang, Y.; Chen, Z.; Han, P.; Du, Y.; Gu, Z.; Xu, X.; Zheng, G. Single-Atomic Cu with Multiple Oxygen Vacancies on Ceria for Electrocatalytic CO₂ Reduction to CH₄. *ACS Catal.* **2018**, *8*, 7113–7119. [[CrossRef](#)]
88. Back, S.; Jung, Y. TiC- and TiN-Supported Single-Atom Catalysts for Dramatic Improvements in CO₂ Electrochemical Reduction to CH₄. *ACS Energy Lett.* **2017**, *2*, 969–975. [[CrossRef](#)]
89. Back, S.; Lim, J.; Kim, N.-Y.; Kim, Y.-H.; Jung, Y. Single-atom catalysts for CO₂ electroreduction with significant activity and selectivity improvements. *Chem. Sci.* **2017**, *8*, 1090–1096. [[CrossRef](#)]
90. Cheng, M.-J.; Clark, E.L.; Pham, H.H.; Bell, A.T.; Head-Gordon, M. Quantum Mechanical Screening of Single-Atom Bimetallic Alloys for the Selective Reduction of CO₂ to C₁ Hydrocarbons. *ACS Catal.* **2016**, *6*, 7769–7777. [[CrossRef](#)]
91. Wang, X.Q.; Chen, Z.; Zhao, X.Y.; Yao, T.; Chen, W.X.; You, R.; Zhao, C.M.; Wu, G.; Wang, J.; Huang, W.X.; et al. Regulation of Coordination Number over Single Co Sites: Triggering the Efficient Electroreduction of CO₂. *Angew. Chem. Int. Ed.* **2018**, *57*, 1944–1948. [[CrossRef](#)] [[PubMed](#)]
92. Pan, F.; Zhang, H.; Liu, K.; Cullen, D.; More, K.; Wang, M.; Feng, Z.; Wang, G.; Wu, G.; Li, Y. Unveiling Active Sites of CO₂ Reduction on Nitrogen-Coordinated and Atomically Dispersed Iron and Cobalt Catalysts. *ACS Catal.* **2018**, *8*, 3116–3122. [[CrossRef](#)]
93. Zhang, C.; Yang, S.; Wu, J.; Liu, M.; Yazdi, S.; Ren, M.; Sha, J.; Zhong, J.; Nie, K.; Jalilov, A.S.; et al. Electrochemical CO₂ reduction with atomic iron-dispersed on nitrogen-doped graphene. *Adv. Energy Mater.* **2018**, *8*, 1703487. [[CrossRef](#)]
94. Liu, X.; Dai, L. Carbon-based metal-free catalysts. *Nat. Rev. Mater.* **2016**, *1*, 16064. [[CrossRef](#)]
95. Asefa, T. Metal-Free and Noble Metal-Free Heteroatom-Doped Nanostructured Carbons as Prospective Sustainable Electrocatalysts. *Acc. Chem. Res.* **2016**, *49*, 1873–1883. [[CrossRef](#)]
96. Duan, X.; Xu, J.; Wei, Z.; Ma, J.; Guo, S.; Wang, S.; Liu, H.; Dou, S. Metal-Free Carbon Materials for CO₂ Electrochemical Reduction. *Adv. Mater.* **2017**, *29*, 1701784. [[CrossRef](#)]
97. Guo, D.; Shibuya, R.; Akiba, C.; Saji, S.; Kondo, T.; Nakamura, J. Active sites of nitrogen-doped carbon materials for oxygen reduction reaction clarified using model catalysts. *Science* **2016**, *351*, 361–365. [[CrossRef](#)]
98. Xu, J.; Kan, Y.; Huang, R.; Zhang, B.; Wang, B.; Wu, K.-H.; Lin, Y.; Sun, X.; Li, Q.; Centi, G.; et al. Revealing the Origin of Activity in Nitrogen-Doped Nanocarbons towards Electrocatalytic Reduction of Carbon Dioxide. *ChemSusChem* **2016**, *9*, 1085–1089. [[CrossRef](#)]
99. Wu, J.; Yadav, R.M.; Liu, M.; Sharma, P.P.; Tiwary, C.S.; Ma, L.; Zou, X.; Zhou, X.-D.; Yakobson, B.I.; Lou, J.; et al. Achieving Highly Efficient, Selective, and Stable CO₂ Reduction on Nitrogen-Doped Carbon Nanotubes. *ACS Nano* **2015**, *9*, 5364–5371. [[CrossRef](#)]
100. Sharma, P.P.; Wu, J.; Yadav, R.M.; Liu, M.; Wright, C.J.; Tiwary, C.S.; Yakobson, B.I.; Lou, J.; Ajayan, P.M.; Zhou, X.-D. Nitrogen-Doped Carbon Nanotube Arrays for High-Efficiency Electrochemical Reduction of CO₂: On the Understanding of Defects, Defect Density, and Selectivity. *Angew. Chem. Int. Ed.* **2015**, *54*, 13701–13705. [[CrossRef](#)]
101. Wu, J.; Liu, M.; Sharma, P.P.; Yadav, R.M.; Ma, L.; Yang, Y.; Zou, X.; Zhou, X.-D.; Vajtai, R.; Yakobson, B.I.; et al. Incorporation of Nitrogen Defects for Efficient Reduction of CO₂ via Two-Electron Pathway on Three-Dimensional Graphene Foam. *Nano Lett.* **2016**, *16*, 466–470. [[CrossRef](#)] [[PubMed](#)]

102. Liu, Y.; Chen, S.; Quan, X.; Yu, H. Efficient Electrochemical Reduction of Carbon Dioxide to Acetate on Nitrogen-Doped Nanodiamond. *J. Am. Chem. Soc.* **2015**, *137*, 11631–11636. [[CrossRef](#)] [[PubMed](#)]
103. Li, W.; Seredych, M.; Rodríguez-Castellón, E.; Bandoz, T.J. Metal-free Nanoporous Carbon as a Catalyst for Electrochemical Reduction of CO₂ to CO and CH₄. *ChemSusChem* **2016**, *9*, 606–616. [[CrossRef](#)] [[PubMed](#)]
104. Sreekanth, N.; Nazrulla, M.A.; Vineesh, T.V.; Sailaja, K.; Phani, K.L. Metal-free boron-doped graphene for selective electroreduction of carbon dioxide to formic acid/formate. *Chem. Commun.* **2015**, *51*, 16061–16064. [[CrossRef](#)] [[PubMed](#)]
105. Qin, Y.; Wen, J.; Zheng, L.; Yan, H.; Jiao, L.; Wang, X.; Cai, X.; Wu, Y.; Chen, G.; Chen, L.; et al. Single-Atom-Based Heterojunction Coupling with Ion-Exchange Reaction for Sensitive Photoelectrochemical Immunoassay. *Nano Lett.* **2021**, *21*, 1879–1887. [[CrossRef](#)]
106. Wu, J.; Sharifi, T.; Gao, Y.; Zhang, T.; Ajayan, P.M. Emerging Carbon-Based Heterogeneous Catalysts for Electrochemical Reduction of Carbon Dioxide into Value-Added Chemicals. *Adv. Mater.* **2019**, *31*, 1804257. [[CrossRef](#)] [[PubMed](#)]
107. Wang, H.; Chen, Y.; Hou, X.; Ma, C.; Tan, T. Nitrogen-doped graphenes as efficient electrocatalysts for the selective reduction of carbon dioxide to formate in aqueous solution. *Green Chem.* **2016**, *18*, 3250–3256. [[CrossRef](#)]
108. Sun, X.; Kang, X.; Zhu, Q.; Ma, J.; Yang, G.; Liu, Z.; Han, B. Very highly efficient reduction of CO₂ to CH₄ using metal-free N-doped carbon electrodes. *Chem. Sci.* **2016**, *7*, 2883–2887. [[CrossRef](#)] [[PubMed](#)]
109. Wang, H.; Jia, J.; Song, P.; Wang, Q.; Li, D.; Min, S.; Qian, C.; Wang, L.; Li, Y.F.; Ma, C.; et al. Efficient Electrocatalytic Reduction of CO₂ by Nitrogen-Doped Nanoporous Carbon/Carbon Nanotube Membranes: A Step Towards the Electrochemical CO₂ Refinery. *Angew. Chemie Int. Ed.* **2017**, *56*, 7847–7852. [[CrossRef](#)]
110. Liu, S.; Yang, H.; Huang, X.; Liu, L.; Cai, W.; Gao, J.; Li, X.; Zhang, T.; Huang, Y.; Liu, B. Identifying Active Sites of Nitrogen-Doped Carbon Materials for the CO₂ Reduction Reaction. *Adv. Funct. Mater.* **2018**, *28*, 1800499. [[CrossRef](#)]
111. Wang, X.; Liu, Y.; Zhu, D.; Zhang, L.; Ma, H.; Yao, N.; Zhang, B. Controllable Growth, Structure, and Low Field Emission of Well-Aligned CN_x Nanotubes. *J. Phys. Chem. B* **2002**, *106*, 2186–2190. [[CrossRef](#)]
112. Zhang, L.; Xiao, J.; Wang, H.; Shao, M. Carbon-Based Electrocatalysts for Hydrogen and Oxygen Evolution Reactions. *ACS Catal.* **2017**, *7*, 7855–7865. [[CrossRef](#)]
113. Zhang, S.; Kang, P.; Ubnoske, S.; Brennaman, M.K.; Song, N.; House, R.L.; Glass, J.T.; Meyer, T.J. Polyethylenimine-Enhanced Electrocatalytic Reduction of CO₂ to Formate at Nitrogen-Doped Carbon Nanomaterials. *J. Am. Chem. Soc.* **2014**, *136*, 7845–7848. [[CrossRef](#)] [[PubMed](#)]
114. Barton Cole, E.; Lakkaraju, P.S.; Rampulla, D.M.; Morris, A.J.; Abelev, E.; Bocarsly, A.B. Using a One-Electron Shuttle for the Multi-electron Reduction of CO₂ to Methanol: Kinetic, Mechanistic, and Structural Insights. *J. Am. Chem. Soc.* **2010**, *132*, 11539–11551. [[CrossRef](#)] [[PubMed](#)]
115. Pels, J.R.; Kapteijn, F.; Moulijn, J.A.; Zhu, Q.; Thomas, K.M. Evolution of nitrogen functionalities in carbonaceous materials during pyrolysis. *Carbon N. Y.* **1995**, *33*, 1641–1653. [[CrossRef](#)]
116. Wang, S.; Zhang, L.; Xia, Z.; Roy, A.; Chang, D.W.; Baek, J.-B.; Dai, L. BCN Graphene as Efficient Metal-Free Electrocatalyst for the Oxygen Reduction Reaction. *Angew. Chem. Int. Ed.* **2012**, *51*, 4209–4212. [[CrossRef](#)]
117. Zhang, L.; Niu, J.; Dai, L.; Xia, Z. Effect of Microstructure of Nitrogen-Doped Graphene on Oxygen Reduction Activity in Fuel Cells. *Langmuir* **2012**, *28*, 7542–7550. [[CrossRef](#)]
118. Gong, K.; Du, F.; Xia, Z.; Durstock, M.; Dai, L. Nitrogen-Doped Carbon Nanotube Arrays with High Electrocatalytic Activity for Oxygen Reduction. *Science* **2009**, *323*, 760–764. [[CrossRef](#)]
119. Zhang, L.; Xia, Z. Mechanisms of Oxygen Reduction on Nitrogen-Doped Graphene for Fuel Cells. *J. Phys. Chem. C* **2011**, *115*, 11170–11176. [[CrossRef](#)]
120. Winther-Jensen, B.; Winther-Jensen, O.; Forsyth, M.; MacFarlane, D.R. High Rates of Oxygen Reduction over a Vapor Phase-Polymerized PEDOT Electrode. *Science* **2008**, *321*, 671–674. [[CrossRef](#)]
121. Ma, C.; Hou, P.; Wang, X.; Wang, Z.; Li, W.; Kang, P. Carbon nanotubes with rich pyridinic nitrogen for gas phase CO₂ electroreduction. *Appl. Catal. B Environ.* **2019**, *250*, 347–354. [[CrossRef](#)]
122. Hawecker, J.; Lehn, J.-M.; Ziessel, R. Electrocatalytic reduction of carbon dioxide mediated by Re(bipy)(CO)₃ Cl (bipy = 2,2'-bipyridine). *J. Chem. Soc. Chem. Commun.* **1984**, 328–330. [[CrossRef](#)]
123. Becker, J.Y.; Vainas, B.; Eger, R.; Kaufman, L. Electrocatalytic reduction of CO₂ to oxalate by Ag II and Pd II porphyrins. *J. Chem. Soc. Chem. Commun.* **1985**, 1471–1472. [[CrossRef](#)]
124. Lu, X.; Ahsaine, H.A.; Dereli, B.; Garcia-Esparza, A.T.; Reinhard, M.; Shinagawa, T.; Li, D.; Adil, K.; Tchalala, M.R.; Kroll, T.; et al. Operando Elucidation on the Working State of Immobilized Fluorinated Iron Porphyrin for Selective Aqueous Electroreduction of CO₂ to CO. *ACS Catal.* **2021**, *11*, 6499–6509. [[CrossRef](#)]
125. Kornienko, N.; Zhao, Y.; Kley, C.S.; Zhu, C.; Kim, D.; Lin, S.; Chang, C.J.; Yaghi, O.M.; Yang, P. Metal–Organic Frameworks for Electrocatalytic Reduction of Carbon Dioxide. *J. Am. Chem. Soc.* **2015**, *137*, 14129–14135. [[CrossRef](#)]
126. Lin, S.; Diercks, C.S.; Zhang, Y.-B.; Kornienko, N.; Nichols, E.M.; Zhao, Y.; Paris, A.R.; Kim, D.; Yang, P.; Yaghi, O.M.; et al. Covalent organic frameworks comprising cobalt porphyrins for catalytic CO₂ reduction in water. *Science* **2015**, *349*, 1208–1213. [[CrossRef](#)]
127. Shen, J.; Kortlever, R.; Kas, R.; Birdja, Y.Y.; Diaz-Morales, O.; Kwon, Y.; Ledezma-Yanez, I.; Schouten, K.J.P.; Mul, G.; Koper, M.T.M. Electrocatalytic reduction of carbon dioxide to carbon monoxide and methane at an immobilized cobalt protoporphyrin. *Nat. Commun.* **2015**, *6*, 8177. [[CrossRef](#)]

128. Mohamed, E.A.; Zahran, Z.N.; Naruta, Y. Efficient electrocatalytic CO₂ reduction with a molecular cofacial iron porphyrin dimer. *Chem. Commun.* **2015**, *51*, 16900–16903. [[CrossRef](#)]
129. Weng, Z.; Jiang, J.; Wu, Y.; Wu, Z.; Guo, X.; Materna, K.L.; Liu, W.; Batista, V.S.; Brudvig, G.W.; Wang, H. Electrochemical CO₂ Reduction to Hydrocarbons on a Heterogeneous Molecular Cu Catalyst in Aqueous Solution. *J. Am. Chem. Soc.* **2016**, *138*, 8076–8079. [[CrossRef](#)]
130. Bhugun, I.; Lexa, D.; Savéant, J.-M. Catalysis of the Electrochemical Reduction of Carbon Dioxide by Iron(0) Porphyrins: Synergistic Effect of Weak Brønsted Acids. *J. Am. Chem. Soc.* **1996**, *118*, 1769–1776. [[CrossRef](#)]
131. Bhugun, I.; Lexa, D.; Saveant, J.-M. Ultraefficient selective homogeneous catalysis of the electrochemical reduction of carbon dioxide by an iron(0) porphyrin associated with a weak Broensted acid cocatalyst. *J. Am. Chem. Soc.* **1994**, *116*, 5015–5016. [[CrossRef](#)]
132. Bhugun, I.; Lexa, D.; Savéant, J.-M. Catalysis of the Electrochemical Reduction of Carbon Dioxide by Iron(0) Porphyrins. Synergistic Effect of Lewis Acid Cations. *J. Phys. Chem.* **1996**, *100*, 19981–19985. [[CrossRef](#)]
133. Aoi, S.; Mase, K.; Ohkubo, K.; Fukuzumi, S. Selective electrochemical reduction of CO₂ to CO with a cobalt chlorin complex adsorbed on multi-walled carbon nanotubes in water. *Chem. Commun.* **2015**, *51*, 10226–10228. [[CrossRef](#)] [[PubMed](#)]
134. Mashiko, T.; Reed, C.A.; Haller, K.J.; Scheidt, W.R. Nature of iron(I) and iron(0) tetraphenylporphyrin complexes. Synthesis and molecular structure of (dibenzo-18-crown-6)bis(tetrahydrofuran)sodium (meso-tetraphenylporphinato)ferrate and bis[tris(tetrahydrofuran)sodium] (meso-tetraphenylporphinato)ferrate. *Inorg. Chem.* **1984**, *23*, 3192–3196. [[CrossRef](#)]
135. Hammouche, M.; Lexa, D.; Savéant, J.M.; Momenteau, M. Catalysis of the electrochemical reduction of carbon dioxide by iron(“0”) porphyrins. *J. Electroanal. Chem. Interfacial Electrochem.* **1988**, *249*, 347–351. [[CrossRef](#)]
136. Hammouche, M.; Lexa, D.; Momenteau, M.; Saveant, J.M. Chemical catalysis of electrochemical reactions. Homogeneous catalysis of the electrochemical reduction of carbon dioxide by iron(“0”) porphyrins. Role of the addition of magnesium cations. *J. Am. Chem. Soc.* **1991**, *113*, 8455–8466. [[CrossRef](#)]
137. Costentin, C.; Drouet, S.; Robert, M.; Savéant, J.-M. A Local Proton Source Enhances CO₂ Electroreduction to CO by a Molecular Fe Catalyst. *Science* **2012**, *338*, 90–94. [[CrossRef](#)]
138. Jeoung, J.-H.; Dobbek, H. Carbon Dioxide Activation at the Ni,Fe-Cluster of Anaerobic Carbon Monoxide Dehydrogenase. *Science* **2007**, *318*, 1461–1464. [[CrossRef](#)]
139. Shin, W.; Lee, S.H.; Shin, J.W.; Lee, S.P.; Kim, Y. Highly Selective Electrocatalytic Conversion of CO₂ to CO at –0.57 V (NHE) by Carbon Monoxide Dehydrogenase from *Moorella thermoacetica*. *J. Am. Chem. Soc.* **2003**, *125*, 14688–14689. [[CrossRef](#)]
140. Naruta, Y.; Sasayama, M.; Sasaki, T. Oxygen Evolution by Oxidation of Water with Manganese Porphyrin Dimers. *Angew. Chemie Int. Ed. English* **1994**, *33*, 1839–1841. [[CrossRef](#)]
141. Atoguchi, T.; Aramata, A.; Kazusaka, A.; Enyo, M. Cobalt(II)–tetraphenylporphyrin–pyridine complex fixed on a glassy carbon electrode and its prominent catalytic activity for reduction of carbon dioxide. *J. Chem. Soc. Chem. Commun.* **1991**, 156–157. [[CrossRef](#)]
142. Yoshida, T.; Kamato, K.; Tsukamoto, M.; Iida, T.; Schlettwein, D.; Wöhrle, D.; Kaneko, M. Selective electrocatalysis for CO₂ reduction in the aqueous phase using cobalt phthalocyanine/poly-4-vinylpyridine modified electrodes. *J. Electroanal. Chem.* **1995**, *385*, 209–225. [[CrossRef](#)]
143. Tanaka, H.; Aramata, A. Aminopyridyl cation radical method for bridging between metal complex and glassy carbon: Cobalt(II) tetraphenylporphyrin bonded on glassy carbon for enhancement of CO₂ electroreduction. *J. Electroanal. Chem.* **1997**, *437*, 29–35. [[CrossRef](#)]
144. Zhou, X.; Micheroni, D.; Lin, Z.; Poon, C.; Li, Z.; Lin, W. Graphene-Immobilized fac-Re(bipy)(CO)₃ Cl for Syngas Generation from Carbon Dioxide. *ACS Appl. Mater. Interfaces* **2016**, *8*, 4192–4198. [[CrossRef](#)]
145. Wang, R.; Haspel, H.; Pustovarenko, A.; Dikhtiarenko, A.; Russkikh, A.; Shterk, G.; Osadchii, D.; Ould-Chikh, S.; Ma, M.; Smith, W.A.; et al. Maximizing Ag Utilization in High-Rate CO₂ Electrochemical Reduction with a Coordination Polymer-Mediated Gas Diffusion Electrode. *ACS Energy Lett.* **2019**, *4*, 2024–2031. [[CrossRef](#)]
146. Sun, X.; Suarez, A.I.O.; Meijerink, M.; van Deelen, T.; Ould-Chikh, S.; Zečević, J.; de Jong, K.P.; Kapteijn, F.; Gascon, J. Manufacture of highly loaded silica-supported cobalt Fischer–Tropsch catalysts from a metal organic framework. *Nat. Commun.* **2017**, *8*, 1680. [[CrossRef](#)]
147. Sun, X.; Olivos-Suarez, A.I.; Osadchii, D.; Romero, M.J.V.; Kapteijn, F.; Gascon, J. Single cobalt sites in mesoporous N-doped carbon matrix for selective catalytic hydrogenation of nitroarenes. *J. Catal.* **2018**, *357*, 20–28. [[CrossRef](#)]
148. Sun, X.; Olivos-Suarez, A.I.; Oar-Arteta, L.; Rozhko, E.; Osadchii, D.; Bavykina, A.; Kapteijn, F.; Gascon, J. Metal-Organic Framework Mediated Cobalt/Nitrogen-Doped Carbon Hybrids as Efficient and Chemoselective Catalysts for the Hydrogenation of Nitroarenes. *ChemCatChem* **2017**, *9*, 1854–1862. [[CrossRef](#)]
149. Santos, V.P.; Wezendonk, T.A.; Jaén, J.J.D.; Dugulan, A.I.; Nasalevich, M.A.; Islam, H.-U.; Chojecki, A.; Sartipi, S.; Sun, X.; Hakeem, A.A.; et al. Metal organic framework-mediated synthesis of highly active and stable Fischer–Tropsch catalysts. *Nat. Commun.* **2015**, *6*, 6451. [[CrossRef](#)]
150. Oar-Arteta, L.; Wezendonk, T.; Sun, X.; Kapteijn, F.; Gascon, J. Metal organic frameworks as precursors for the manufacture of advanced catalytic materials. *Mater. Chem. Front.* **2017**, *1*, 1709–1745. [[CrossRef](#)]
151. Lu, X.; Wu, Y.; Yuan, X.; Huang, L.; Wu, Z.; Xuan, J.; Wang, Y.; Wang, H. High-Performance Electrochemical CO₂ Reduction Cells Based on Non-noble Metal Catalysts. *ACS Energy Lett.* **2018**, *3*, 2527–2532. [[CrossRef](#)]

152. Morlanés, N.; Takanabe, K.; Rodionov, V. Simultaneous Reduction of CO₂ and Splitting of H₂O by a Single Immobilized Cobalt Phthalocyanine Electrocatalyst. *ACS Catal.* **2016**, *6*, 3092–3095. [[CrossRef](#)]
153. Kramer, W.W.; McCrory, C.C.L. Polymer coordination promotes selective CO₂ reduction by cobalt phthalocyanine. *Chem. Sci.* **2016**, *7*, 2506–2515. [[CrossRef](#)] [[PubMed](#)]
154. Abe, T.; Yoshida, T.; Tokita, S.; Taguchi, F.; Imaaya, H.; Kaneko, M. Factors affecting selective electrocatalytic CO₂ reduction with cobalt phthalocyanine incorporated in a polyvinylpyridine membrane coated on a graphite electrode. *J. Electroanal. Chem.* **1996**, *412*, 125–132. [[CrossRef](#)]
155. Lieber, C.M.; Lewis, N.S. Catalytic reduction of carbon dioxide at carbon electrodes modified with cobalt phthalocyanine. *J. Am. Chem. Soc.* **1984**, *106*, 5033–5034. [[CrossRef](#)]
156. Liu, Y.; McCrory, C.C.L. Modulating the mechanism of electrocatalytic CO₂ reduction by cobalt phthalocyanine through polymer coordination and encapsulation. *Nat. Commun.* **2019**, *10*, 1683. [[CrossRef](#)]
157. Wang, X.; Cai, Z.; Wang, Y.; Feng, Y.; Yan, H.; Wang, D.; Wan, L. In Situ Scanning Tunneling Microscopy of Cobalt-Phthalocyanine-Catalyzed CO₂ Reduction Reaction. *Angew. Chem. Int. Ed.* **2020**, *59*, 16098–16103. [[CrossRef](#)]
158. Zhang, X.; Wu, Z.; Zhang, X.; Li, L.; Li, Y.; Xu, H.; Li, X.; Yu, X.; Zhang, Z.; Liang, Y.; et al. Highly selective and active CO₂ reduction electrocatalysts based on cobalt phthalocyanine/carbon nanotube hybrid structures. *Nat. Commun.* **2017**, *8*, 14675. [[CrossRef](#)]
159. Latiff, N.M.; Fu, X.; Mohamed, D.K.; Veksha, A.; Handayani, M.; Lisak, G. Carbon based copper(II) phthalocyanine catalysts for electrochemical CO₂ reduction: Effect of carbon support on electrocatalytic activity. *Carbon N. Y.* **2020**, *168*, 245–253. [[CrossRef](#)]
160. Mei, B.; Liu, C.; Li, J.; Gu, S.; Du, X.; Lu, S.; Song, F.; Xu, W.; Jiang, Z. Operando HERFD-XANES and surface sensitive Δμ analyses identify the structural evolution of copper(II) phthalocyanine for electroreduction of CO₂. *J. Energy Chem.* **2022**, *64*, 1–7. [[CrossRef](#)]
161. Kusama, S.; Saito, T.; Hashiba, H.; Sakai, A.; Yotsuhashi, S. Crystalline Copper(II) Phthalocyanine Catalysts for Electrochemical Reduction of Carbon Dioxide in Aqueous Media. *ACS Catal.* **2017**, *7*, 8382–8385. [[CrossRef](#)]
162. Acharjya, S.; Chen, J.; Zhu, M.; Peng, C. Elucidating the reactivity and nature of active sites for tin phthalocyanine during CO₂ reduction. *Greenh. Gases Sci. Technol.* **2021**, *11*, 1191–1197. [[CrossRef](#)]
163. Zhang, X.; Wang, Y.; Gu, M.; Wang, M.; Zhang, Z.; Pan, W.; Jiang, Z.; Zheng, H.; Lucero, M.; Wang, H.; et al. Molecular engineering of dispersed nickel phthalocyanines on carbon nanotubes for selective CO₂ reduction. *Nat. Energy* **2020**, *5*, 684–692. [[CrossRef](#)]
164. Li, X.; Chai, G.; Xu, X.; Liu, J.; Zhong, Z.; Cao, A.; Tao, Z.; You, W.; Kang, L. Electrocatalytic reduction of CO₂ to CO over iron phthalocyanine-modified graphene nanocomposites. *Carbon N. Y.* **2020**, *167*, 658–667. [[CrossRef](#)]
165. Zheng, J.; Li, X.; Qin, Y.; Zhang, S.; Sun, M.; Duan, X.; Sun, H.; Li, P.; Wang, S. Zn phthalocyanine/carbon nitride heterojunction for visible light photoelectrocatalytic conversion of CO₂ to methanol. *J. Catal.* **2019**, *371*, 214–223. [[CrossRef](#)]
166. Zhang, W.; Hu, Y.; Ma, L.; Zhu, G.; Wang, Y.; Xue, X.; Chen, R.; Yang, S.; Jin, Z. Progress and perspective of electrocatalytic CO₂ reduction for renewable carbonaceous fuels and chemicals. *Adv. Sci.* **2018**, *5*, 1700275. [[CrossRef](#)]